ERDC/EL TR-08-34

Environmental Laboratory

US Army Corps
of Engineers®
Engineer Research and
Development Center

Environmental Quality and Installations Program

UXO Characterization: Comparing Cued Surveying to Standard Detection and Discrimination Approaches

Report 3 of 9
Test Stand Magnetic and Electromagnetic Measurements of Unexploded Ordnance

Stephen D. Billings, Leonard R. Pasion, Sean Walker, and Cathy Pasion

September 2008

UXO Characterization: Comparing Cued Surveying to Standard Detection and Discrimination Approaches

Report 3 of 9
Test Stand Magnetic and Electromagnetic Measurements of Unexploded Ordnance

Stephen D. Billings, Leonard R. Pasion, Sean Walker, and Cathy Pasion

Sky Research, Inc.
445 Dead Indian Memorial Road
Ashland, OR 97520-9706

Report 3 of 9

Approved for public release; distribution is unlimited.

Abstract: This report describes a test stand data collection program that was designed to provide the highest possible quality magnetic and electro-magnetic data over a suite of ordnance and calibration items. Each of the data points was precisely positioned and oriented, had low signal-to-noise ratio, and had minimal response from cultural or geologic sources. The test stand facility is described and an overview of the various geophysical instruments deployed, a description of the ordnance items measured, and a discussion of survey design and data collection are provided. Examples of how the data have been used in other parts of the overarching research project are also provided.

Test stand data were collected using a Geometrics G822 cesium vapor magnetometer, Geonics EM-61 and EM-63 time-domain metal detectors, and a Geophex GEM-3 frequency-domain detector. Measured items included 20-, 37-, 40-, 57-, 76-, 90-, and 155-millimeter (mm) projectiles, a 2.75-in. rocket, 60- and 81-mm mortars, BLU-26, BLU28, MK118 Rockeye and M42 submunitions, a 40-mm grenade, and a 105-mm HEAT round. A number of iron and aluminum cylinders, both hollow and solid, of different aspect ratio were also measured.

This is Report 3 in a series of nine reports prepared under project W912HZ-04-C-0039 "UXO Characterization: Comparison of Cued Surveying to Standard Detection and Standard Discrimination Approaches."

Contents

Report Documentation Page

Figures and Tables

Figures

Tables

Preface

This report was prepared as part of the Congressional Interest Environmental Quality and Installations Program, Unexploded Ordnance (UXO) Focus Area, Contract No. W912HZ-04-C-0039, Purchase Request No. W81EWF418-0425, titled, "UXO Characterization: Comparison of Cued Surveying to Standard Detection and Standard Discrimination Approaches." Research was conducted by Sky Research, Inc., for the Environmental Laboratory (EL), U.S. Army Engineer Research and Development Center (ERDC), Vicksburg, MS. The following Sky Research personnel contributed to this report:

- Dr. Stephen D. Billings was the project Principal Investigator, oversaw the data collection and analysis of the field data, and produced the report for this segment of the project;
- Dr. Leonard R. Pasion conducted quality control of the parametric inversions;
- Sean Walker and Cathy Pasion assisted with the data collection and processing of the data;
- Joy Rogalla was the copy editor for this report.

This project was performed under the general supervision of Dr. M. John Cullinane, Jr., Technical Director, Military Environmental Engineering and Sciences, EL; and John H. Ballard, Office of Technical Director and UXO Focus Area Manager, EL. Reviews were provided by Mr. Ballard and Dr. Dwain Butler, Alion Science and Technology Corporation. Dr. Beth Fleming was Director, EL.

COL Gary E. Johnston was Commander and Executive Director of ERDC. Dr. James R. Houston was Director.

Acknowledgments

Unit Conversion Factors

Multiply	By	To Obtain
feet	0.3048	meters

Acronyms

A	amperes
ASCII	American Standard Code for Information Interchange
ATC	Aberdeen Test Center
cm	centimeter(s)
DoD	Department of Defense
DSB	Defense Science Board
EM	Electromagnetic
EMI	Electromagnetic Induction
ERDC	Engineer Research and Development Center
FLBGR	Former Lowry Bombing and Gunnery Range
GPR	Ground Penetrating Radar
Hz	Hertz
in.	inch
kHz	kilohertz
km	kilometer(s)
m	meter(s)
mm	millimeter(s)
µs	microseconds
Ms	millisecond(s)
mV	millivolt
MTANG	Montana Army National Guard
PC	Personal Computer
P-O	Pasion-Oldenburg
ppm	parts per million
SERDP	Strategic Environmental Research and Development Program
SNR	Signal-to-Noise Ratio
UXO	Unexploded Ordnance
USACE	U.S. Army Corps of Engineers

General Introduction

The clearance of military facilities in the United States contaminated with unexploded ordnance (UXO) is one of the most significant environmental concerns facing the Department of Defense (DoD). A 2003 report by the Defense Science Board (DSB) on the topic estimated costs of remediation in the tens of billions of dollars. The DSB recognized that development of effective discrimination strategies to distinguish UXO from non-hazardous material is one essential technology area where the greatest cost saving to DoD can be achieved.

The objective of project W912HZ-04-C-0039 "UXO Characterization: Comparison of Cued Surveying to Standard Detection and Standard Discrimination Approaches," was to research, develop, optimize, and evaluate the efficiencies of different modes of UXO characterization and remediation as a function of the density of UXO and associated clutter. Survey modes investigated in the research include:

1. Standard detection survey: All selected anomalies are excavated;
2. Advanced discrimination survey: Data collected in proximity to each identified anomaly are inverted for physics-based parameters and statistical or analytical classifiers are used to rank anomalies, from which a portion of the higher ranked anomalies are excavated;
3. Cued survey mode: Each selected anomaly is revisited with an interrogation platform, high-quality data are collected and analyzed, and a decision is made as to whether to excavate the item, or leave it in the ground.

Specific technical objectives of the research were to:

* Determine the feasibility and effectiveness of various interrogation approaches based on the cued-survey approach;
* Determine the feasibility and effectiveness of various interrogation sensors including magnetics, ground penetrating radar (GPR), and electromagnetic (EM) induction (EMI), and evaluate combinations of these sensors;
* Develop and evaluate the most promising interrogation platform designs;

- Develop optimal processing and inversion approaches for cued-interrogation platform data sets;
- Evaluate the data requirements to execute accurate target parameterization and assess the technical issues of meeting these requirements using detection and interrogation survey techniques;
- Determine which survey mode is most effective as a function of geological interference, and UXO/clutter density;
- Investigate the feasibility and effectiveness of using detailed test stand measurements on UXO and clutter to assist in the design of interrogation algorithms used in the cued-search mode.

The main areas of research involved in these coordinated activities include:

- Sensor phenomenology including GPR, EMI , and magnetometry;
- Data collection systems; platforms, field survey systems, field interrogation systems;
- Parameter estimation techniques; inversion techniques (single, cooperative, joint), forward-model parameterizations, processing strategies; and
- Classification methods; thresholding, statistical models, information systems.

This report "UXO Characterization: Comparing Cued Surveying to Standard Detection and Discrimination Approaches: Report 3 of 9 – Test Stand Magnetic and Electromagnetic Measurements of Unexploded Ordnance," is one of a series of nine reports written as part of W912HZ-04-C-0039:

1. UXO Characterization: Comparing Cued Surveying to Standard Detection and Discrimination Approaches: Report 1 of 9 – Summary Report;
2. UXO Characterization: Comparing Cued Surveying to Standard Detection and Discrimination Approaches: Report 2 of 9 – Ground Penetrating Radar for Unexploded Ordnance Characterization; Fundamentals;
3. UXO Characterization: Comparing Cued Surveying to Standard Detection and Discrimination Approaches: Report 3 of 9 – Test Stand Magnetic and Electromagnetic Measurements of Unexploded Ordnance;

4. UXO Characterization: Comparing Cued Surveying to Standard Detection and Discrimination Approaches: Report 4 of 9 – UXO Characterization Using Magnetic, Electromagnetic and Ground Penetrating Radar Measurements at the Sky Research Test Plot;

5. UXO Characterization: Comparing Cued Surveying to Standard Detection and Discrimination Approaches: Report 5 of 9 – Optimized Data Collection Platforms and Deployment Modes for Unexploded Ordnance Characterization;

6. UXO Characterization: Comparing Cued Surveying to Standard Detection and Discrimination Approaches: Report 6 of 9 – Advanced Electromagnetic and Magnetic Methods for Discrimination of Unexploded Ordnance;

7. UXO Characterization: Comparing Cued Surveying to Standard Detection and Discrimination Approaches: Report 7 of 9 – Marine Corps Base Camp Lejeune: UXO Characterization Using Ground Penetrating Radar;

8. UXO Characterization: Comparing Cued Surveying to Standard Detection and Discrimination Approaches: Report 8 of 9 – Marine Corps Base Camp Lejeune: UXO Characterization Using Magnetic and Electromagnetic Data;

9. UXO Characterization: Comparing Cued Surveying to Standard Detection and Discrimination Approaches: Report 9 of 9 – Former Lowry Bombing and Gunnery Range: Comparison of UXO Characterization Performance Using Area and Cued-interrogation Survey Modes.

1 Introduction

This research project focused on the development of algorithms, platforms, and deployment modes for efficient discrimination of UXO from non-hazardous clutter. To determine if these modifications lead to performance improvements, a high-quality baseline data set was required. The test stand facility at the Vicksburg site of the USACE-ERDC had just been built when this project started, and it provided the ideal measurement scenario (Figure 1). The test stand is elevated about 3 meters (m) above the ground so that geophysical data can be collected in an environment free of background geologic response. Ordnance and calibration items can be placed at an accurately known position and orientation relative to the geophysical sensor. The sensor is mounted on a robotic arm that is precisely positioned and that can be moved around the test stand using control software running on a personal computer (PC).

Figure 1. View of the ERDC test stand from the north.

A series of three data collection efforts were carried out during March-April 2005, July 2005, and February 2006 using a combination of magnetometers, EM-61, EM-63, and GEM-3 sensors. Chapter 2 of this report describes the test stand measurement procedures, the ordnance and

calibration items that were measured, and the sensors that were deployed. Chapter 3 describes the data processing procedures that were used. Chapter 4 presents some examples of data images and Chapter 5 describes dipole model fits to the data. Chapter 6 discusses instances where the test stand data were used to support different aspects of this research project.

2 Data Collection Procedure

2.1. Measurement plan

During surveying, the motion of the sensor on the platform is determined using an American Standard Code for Information Interchange (ASCII) control file. This file specifies the survey locations and the dwell time at each location. It is possible to survey in both static and dynamic modes. Since the purpose was to obtain high quality data, the test stand was employed in fiducial mode with the sensor stopping for 3 seconds at each measurement location. The survey pattern was varied based on the size of the ordnance being measured and the sensor being used. A more detailed description of survey patterns is presented in Chapter 2.

The positions from a given survey are recorded by the PC controlling the test stand in an ASCII file with the following format: "time," "x," "y." The geophysical sensor data are recorded separately by the particular instrument being used. These sensor data are then exported to an ASCII file that contains the time and data values for each measurement.

The useable area of the test stand is approximately 3 by 4 m. In the local coordinates of the test stand, the southwest corner is defined as (1 m East, 1 m North) and all measurements are relative to this point. An ordnance holder that can be adjusted to a specified depth, dip, and azimuth is located below the deck. The x-y location of the holder for data collected in 2005 was (3.55 m East, 2.56 m North) and the holder location for data collected in 2006 was (3.69 m East, 2.56 m North). The difference was due to modifications made to the test stand between July 2005 and February 2006. During the 2005 surveys, a #8 shot was placed on the deck of the test stand at (1 m East, 1 m North) and was used as a calibration item. When the #8 shot was replaced by a smaller shot permanently mounted below the deck of the test stand, the location of (1 m East, 1 m North) was shifted 14 centimeters (cm) west and, hence, the relative location of the ordnance holder shifted.

2.2. Ordnance measured

The suite of ordnance measured at the test stand was also the set of ordnance destined for burial in the Ashland test plot. The group included

12 items from the Aberdeen Test Center (ATC) Standardized Target Repository, three ordnance from the Montana Army National Guard (MTANG), six UXO simulants and three pieces of shrapnel collected from the Chevallier Ranch site in Montana. For the MTANG and ATC sets, there were three specimens of each UXO item.

The set of items provides a representative cross section of ordnance types from large to small, ferrous to aluminum, and includes projectiles, mortars, and submunitions. All ATC items were inert and have never been fired. A description of the ATC items and their sizes can be found in Table 1.

Table 1. Description of UXO from ATC standardized set measured at the test stand.

Type	Description	Length cm	Diameter cm	Aspect Ratio	Weight lb	L-Large M-Medium S-Small
20-mm	20-mm M55	7.5	2.0	3.75	0.25	S
37-mm	37-mm	12.0	3.7	3.24	1.50	S
40-mm	40-mm M385	8.0	4.0	2.00	0.55	S
M42	Submunition	6.2	4.0	1.55	0.35	S
BLU-26	Submunition	6.6	6.6	1.00	0.95	S
BDU-28	Submunition	9.7	6.7	1.45	1.70	S
MKI18	MK118 Rockeye	34.4	5.0	6.88	1.35	M
60-mm	60-mm M49A3	24.3	6.0	4.05	2.90	M
81-mm	81-mm M374	48.0	8.1	5.93	8.75	M
M230	2.75-in. Rocket	76.1	7.5	10.15	18.20	M
105-mm	M456 Heat Rod	64.0	10.5	6.10	19.65	L
155-mm	155-mm M483AI	87.0	15.5	5.61	56.45	L

The three types of ordnance from the MTANG were all previously fired and consist of two artillery rounds (76-mm and 90-mm) and one mortar (81-mm). These items all represent medium-sized ordnance. A detailed description of the MTANG ordnance can be found in Table 2. The ordnance was recovered from the Chevallier Ranch site, about 25 kilometers (km) north of Helena, MT.

Table 2. Description of the UXO from the Montana Army National Guard measured at the test stand.

Type	Description	Length cm	Diameter cm	Aspect Ratio	Weight lb	L-Large M-Medium S-Small
76-mm	Artillery	22.00	7.60	2.89	13.50	M
81-mm	Mortar	27.30	8.10	3.37	6.00	M
96-mm	Artillery	25.00	9.00	2.78	22.50	M

The group of UXO simulants was comprised of machined cylinders of various lengths and material properties to represent different types of idealized UXO. The cylinders were cut at either 6 or 12 in. The materials used were steel and aluminum. Hollow and solid steel cylinders were machined; however, only solid aluminum cylinders were used. A detailed description of the UXO simulants can be found in Table 3.

Table 3. Description of the UXO simulants measured at the test stand.

Description	Length cm	Outside Diameter cm	Inside Diameter cm	Aspect Ratio	Weight lb	L-Large M-Medium S-Small
12-in. Steel Rod	30.5	7.5	n/a	4.07	24.0	M
6-in. Steel Rod	15.3	7.5	n/a	2.04	12.0	M
12-in. Steel Tubing	30.5	7.5	6.3	4.07	7.5	M
6-in. Steel Tubing	15.2	7.5	6.3	2.03	3.5	M
12-in. Aluminum Rod	30.5	7.5	n/a	4.07	8.5	M
6-in. Aluminum Rod	15.2	7.5	n/a	2.03	4.0	M

The three pieces of shrapnel were obtained from low-order detonations of ordnance collected from the Chevallier Ranch site in Montana. In order to determine the shape and size of the pieces of shrapnel, the items were placed on a flat surface with the convex surface up. The length and width were measured in the plane of the flat surface. The depth was determined by measuring the maximum perpendicular distance from the surface to the outer edge of the ordnance. The measured values for the shrapnel are listed in Table 4.

Table 4. Description of the Montana shrapnel items measured
at the test stand.

Description	Length, cm	Width, cm	Depth, cm
MT Shrapnel 1	23.0	7.0	4.5
MT Shrapnel 2	32.0	15.0	4.5
MT Shrapnel 3	20.0	10.0	4.0

These items make up the full suite of items available for measurement at the test stand.

2.3. Sensors

2.3.1. Time domain electromagnetic induction data

Time domain EM data were collected using the Geonics EM-63, which is a pulsed, multi-channel time domain EMI instrument. The system consists of a 1- by 1-m square transmitter coil and three coaxial 0.5- by 0.5-m square receiver loops. The voltages measured in the receiver loops are averaged over 26 geometrically spaced time gates, spanning the range 180 microseconds (μs) to 25.14 milliseconds (ms). The data from the EM-63 represent the vertical component of $\partial B(r,t)/\partial t$ and are reported in units of millivolts (mV).

A subset of the ordnance was also surveyed with the Geonics EM-61 MKII. Like the EM-63, the EM-61 is a pulsed multi-channel EMI instrument. The transmitter and receiver loops comprise the same 0.5- by 1-m rectangular loop. The EM-61 MKII configuration measured consisted of four time gates spanning the range 400 μs to 3.8 ms. The data from the EM-61 also represent the vertical component of $\partial B(r,t)/\partial t$ and are reported in units of millivolt.

2.3.2. Frequency domain electromagnetic induction data

Frequency domain EM data were collected using the Geophex GEM-3 sensor. The sensor consists of a circular transmitter loop with a diameter of 40 cm and a smaller circular receiver loop located in the center of the transmitter loop. The use of a bucking coil produces a primary field free cavity at the receiver coil. This permits accurate measurements of the secondary field to be made in the presence of a significantly stronger primary field. The GEM-3 data were collected using two different systems. During July 2005 the experimental GEM-3-3D was used, which contains

three mutually orthogonal receiver coils at the center of the transmitter coil. Unfortunately, the data from the x and y coils were intermittent and noisy, and as such they will not be presented or discussed further. During 2006 a standard GEM-3 with a single z receiver coil was used. The data from the GEM-3 are reported as in-phase (real) and quadrature (imaginary) components of the secondary magnetic field in units of parts per million (ppm). The ppm units are defined as the secondary field at the receiver coil normalized by the primary field that would have been measured at the center of the coil (if it had not been bucked out) multiplied by 10^6.

2.3.3. Magnetometer data

Total field magnetometer data were collected at a 10-hertz (Hz) rate using a Geometrics G858 cesium vapor magnetometer. A G-856 proton procession magnetometer was located about 15 m away and monitored temporal changes in the Earth's magnetic field at a 5-Hz rate. No magnetic data are presented in this report. Instead, a paper describing the measurement procedures, the data, and magnetic models of each ordnance item was published in the IEEE Transactions of Geoscience and Remote Sensing (Billings et al. 2006).

2.4. Survey design

In order to maximize measurement detail while minimizing survey time, three grids were defined for measurements of the ATC and Montana ordnance. The three grids, named "deep," "mid," and "shallow," were designed such that the density of the grid pattern at the center of the test stand would increase as the target was brought closer to the surface. The basis for all the grids was a 3- by 3-m grid with 30-cm station spacing. Detailed grids were as follows:

- The deep grid that was used for large and medium-sized targets at depths of 1 m and greater had a 2.1- by 2.1-m detailed area with 15-cm station spacing.
- For mid depth targets (medium and small-sized ordnance at depths of 0.6 to 0.75 m), the grid contained a 2.1- by 2.1-m area populated with stations at 15-cm spacing and a 0.9- by 0.9-m area populated with 7.5-cm station spacing.
- For shallow depth targets (small-sized ordnance and shrapnel at depths less than 0.5 m), the grid contained a 1.4- by 1.4-m area

populated with stations at 10-cm spacing and a 0.5- by 0.5-m area populated with 5-cm station spacing.

Three other grid definitions were used for repeat measurements and for the cylinders. Two 2- by 2-m grids and one 1- by 1-m grid were used:

- The 2- by 2-m "fine" grid (used for cylinder measurements) had 12.5-cm station spacing;
- The 2- by 2-m "coarse" grid (used for repeat measurements of medium and large ordnance and cylinders) had 25-cm station spacing; and
- The 1- by 1-m "fine" grid (used for repeat measurements of small ordnance) had 12.5-cm station spacing.

Images of the grid patterns are shown in Figures 2 and 3.
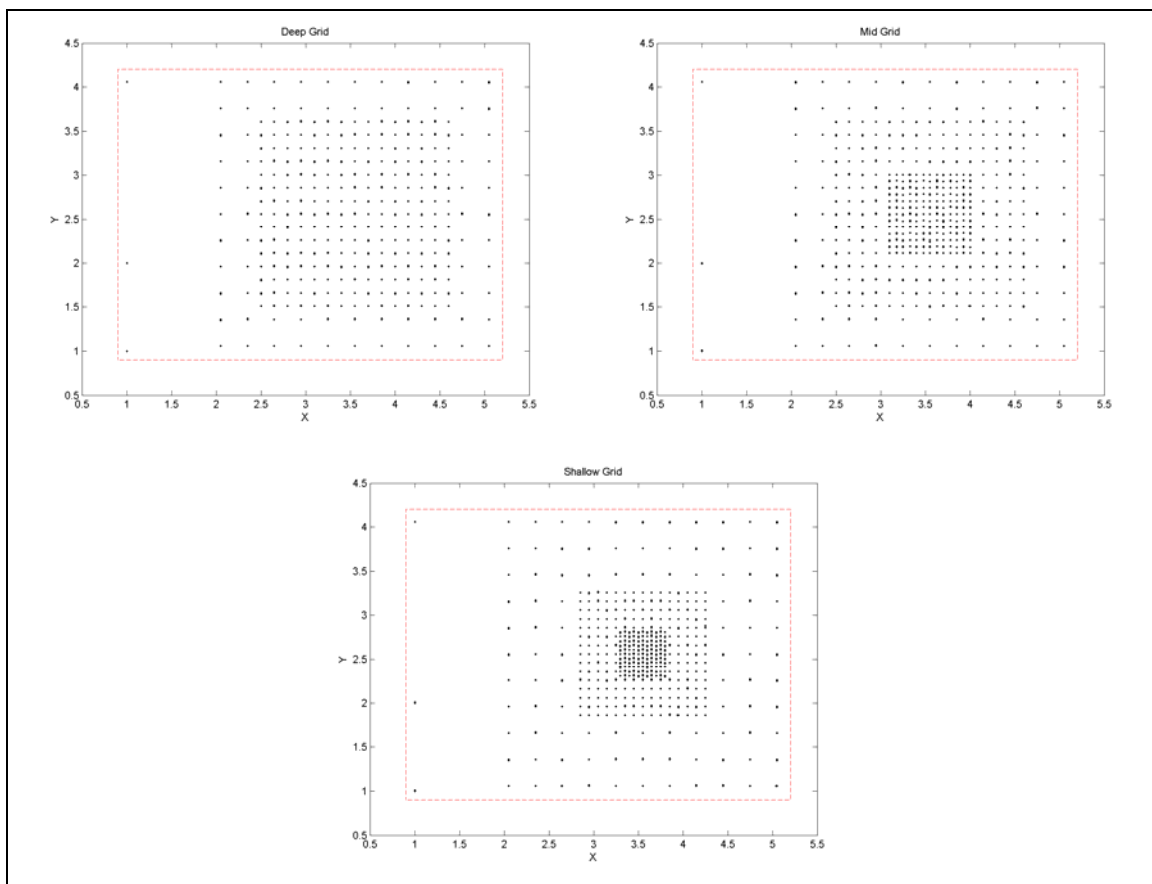
Figure 2. EM-63 survey patterns used for the ATC and Montana items. The top left panel shows the "deep" grid, top right panel shows the "mid" grid, and the bottom panel shows the "shallow" grid.
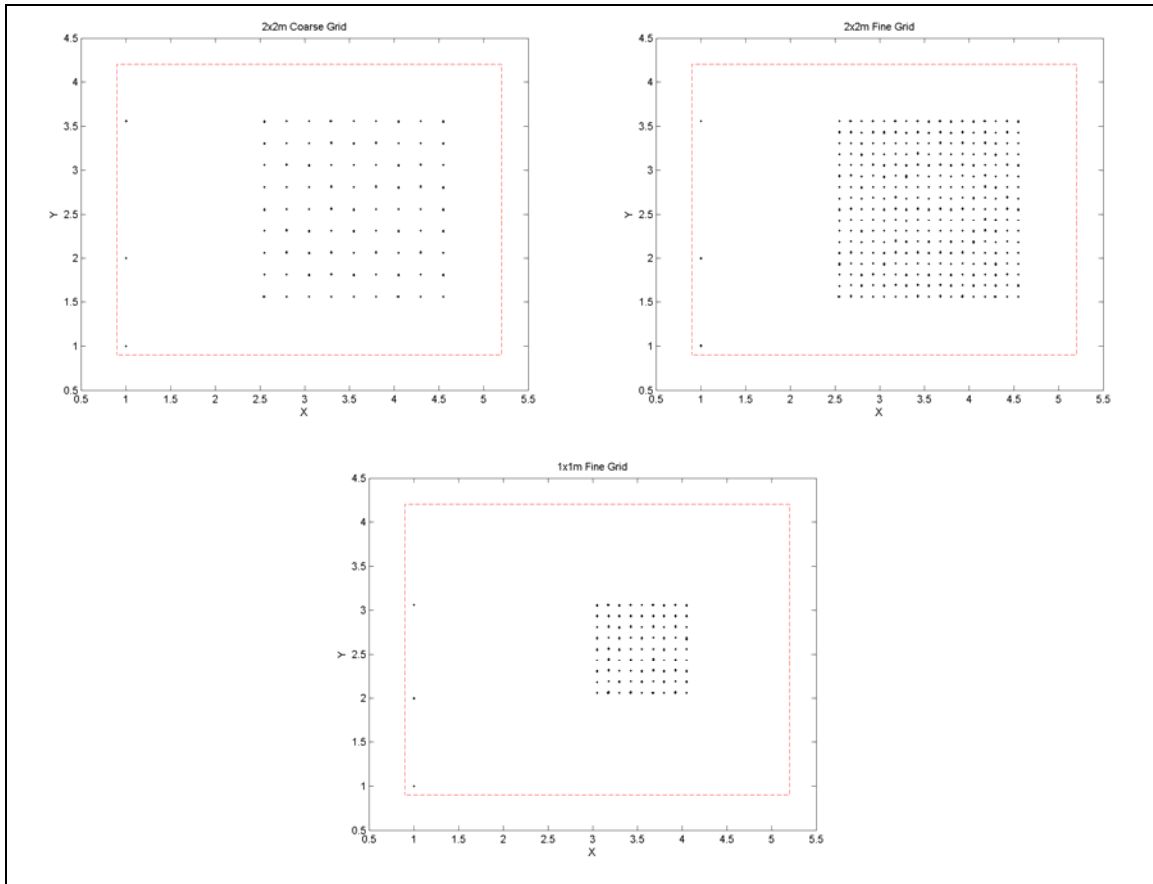
Figure 3. EM-63 survey patterns used for the cylinders and repeat measurements. The top left panel shows the "2 × 2 coarse" grid, top right panel shows the "2 × 2 fine" grid, and the bottom panel shows the "1 × 1 fine" grid.

3 Processing of Test Stand Data

This chapter describes the processing operations applied to the GEM-3, EM-61, and EM-63 data.

3.1. Merging position and sensor data

The first step in processing each data set (regardless of sensor type) was to synchronize the position and sensor data. This was achieved by starting each survey in a consistent manner. Prior to starting the survey measurements, the sensor was positioned over a calibration object located at a known position (a steel shot located at the southwest corner [1 m East, 1 m North] of the test stand). This resulted in a large-amplitude response in the sensor data. The data were synchronized by matching the point in the position file where the sensor moves off of the calibration object with the point where the response of the sensor begins to change. After the two time stamps were synchronized, the position and sensor data were merged by interpolating positions to the measurements. The resulting data file contained spatially located sensor measurements. This step of data processing was time-consuming, since it required the interpreter to select the correct time lag between the sensor and position data.

3.2. Drift correction and background removal

The second and more complex step in processing the test stand data was to apply a correction for time-based drift of the sensor data and the removal of background or system response. Since this process is different for each sensor type they are described individually.

3.2.1. Time domain EM processing, background removal and time-based drift correction

To estimate the drift in the EM-63 response, measurements were performed at location (1 m East, 2 m North) on the grids shown in Figures 2 and 3 at the beginning and end of each survey. Depending upon the length of the survey, the sensor returned to station (1 m East, 2 m North) during the survey to record an intermediate measurement. The drift between these measurements was linearly interpolated and removed from the data. This process was applied to each time channel individually. Since the point (1 m East, 2 m North) was located close to the metal shot at (1 m East, 1 m North)

this point was not used as a background or "zero" value. Instead, the most northwesterly point in the survey grid was selected. This point corresponds to a point far enough away from the shot and the ordnance. The median value of the drift-corrected background data was then subtracted from all of the survey data. In all of the examples shown in this section, only the first time channel of data is shown. In order to drift-correct the data, the same process was performed on each time channel independently.

This scheme appeared to work well with large-amplitude (>100 mV in time channel 1) anomalies. In the case of the approximately 30-mV response from a 20-mm projectile 40 cm below the sensor (Figure 4), the drift-correction method was imperfect. By highlighting the lowest 10 mV of the response (Figure 5), one can see that there is still some drift-related signal in the data. In the case of a weaker response (~12 mV) from a 40-mm projectile at 60 cm, the method appears to be completely inadequate (Figure 6). In both Figures 5 and 6, there is drift-related signal on the order of 7 mV.

By plotting the data in profile, one can see how the response varies with time. Figures 7 and 8 show the unleveled and static leveled data as a function of time for the 20-mm and 40-mm projectiles shown in Figures 4 and 6.

Figure 4. Gridded images of time channel 1 of the unleveled (left) and static leveled (right) test stand measurements over an ATC 20 mm, depth = 40 cm, dip = 45°, and azimuth = 0°. Panel (a) shows the unleveled data and panel (b) shows the data leveled using the static measurements at (1 m East, 2 m North). Units are in millivolts.

Figure 5. Color stretched gridded images of time channel 1 of the unleveled (left) and static leveled (right) test stand measurements over an ATC 20 mm, depth = 40 cm, dip = 45°, and azimuth = 0°. The color bar in both images has been stretched to include only the lowest 10 mV of data. Panel (a) shows the unleveled data and panel (b) shows the data leveled using the static measurements at (1 m East, 2 m North).
Units are in millivolts.
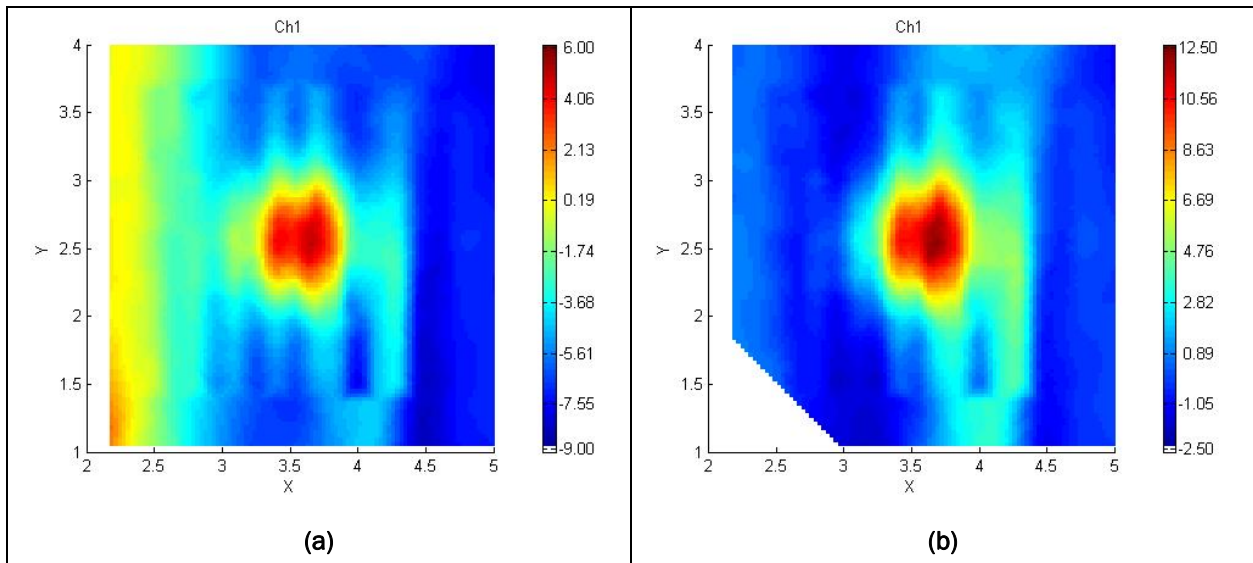
Figure 6. Gridded images of time channel 1 of the unleveled (left) and static leveled (right) test stand measurements over an ATC 40 mm, depth = 60 cm, dip = -90°. and azimuth = 0°. Panel (a) shows the unleveled data and panel (b) shows the data leveled using the background measurements. Units are in millivolts.

Figure 7. Comparison of unleveled data with static leveled data over an ATC 20 mm, depth = 40 cm, dip = 45°, and azimuth = 0°. In the top panel, the black profile is the unleveled channel 1 response as a function of time, the red circles represent static measurements, and the red dotted line is the linearly interpolated values. In the bottom panel the green profile is the static leveled and background corrected response. The channel 1 response is expressed in millivolts and the time is expressed in minutes. Spikes in the data are due to time synch issues within the data; these bad data points are removed during processing.

During the survey over the ATC 20 mm, the time between the first and second static measurement (red circles in Figure 7) was approximately 22 minutes. The gridded data in Figures 4 and 5 and the profile data show that the EM-63 response is drifting on a time scale shorter than 22 minutes. While the drift measurements in Figure 8 are approximately 12 minutes apart, the EM-63 is still drifting significantly. In both cases the static drift correction and background removal are not able to correct for the drift of the EM-63.

One solution to this problem would be to collect drift measurements more often; however, this is not desirable as it would significantly increase the time required to survey each item. Another approach is to assume that the test stand is a source-free environment. Therefore, all data collected at the

Figure 8. Comparison of unleveled data with static leveled data over an ATC 40 mm, depth = 60 cm, dip = -90°, and azimuth = 0°. In the top panel, the black profile is the unleveled channel 1 response as a function of time, the red circles represent static measurements, and the red dotted line is the linearly interpolated values. In the bottom panel the green profile is the static leveled and background corrected response. The channel 1 response is expressed in millivolts and the time is expressed in minutes. The spikes in the data are due to time synch issues within the data; these bad data points are removed during processing.

edge of the test stand are treated as background measurements and, therefore, can be used in drift calculations. Figure 9 contains a plan map showing the data points used in the edge-leveling process. This correction is called "edge leveling." Gridded images of the unleveled and edge-leveled data over the 20-mm and 40-mm projectiles are presented in Figures 10 and 12, respectively. Profiles of unleveled and edge-leveled data over the 20-mm and 40-mm projectiles are presented in Figures 11 and 13, respectively.

Efforts to develop a drift correction scheme based on correlating drift with the transmitter current are described in Appendix A. This procedure was partially successful but did not produce results as consistent as the edge-based scheme described above. Identical edge-based drift correction schemes were used for the EM-61 and for the EM-63.
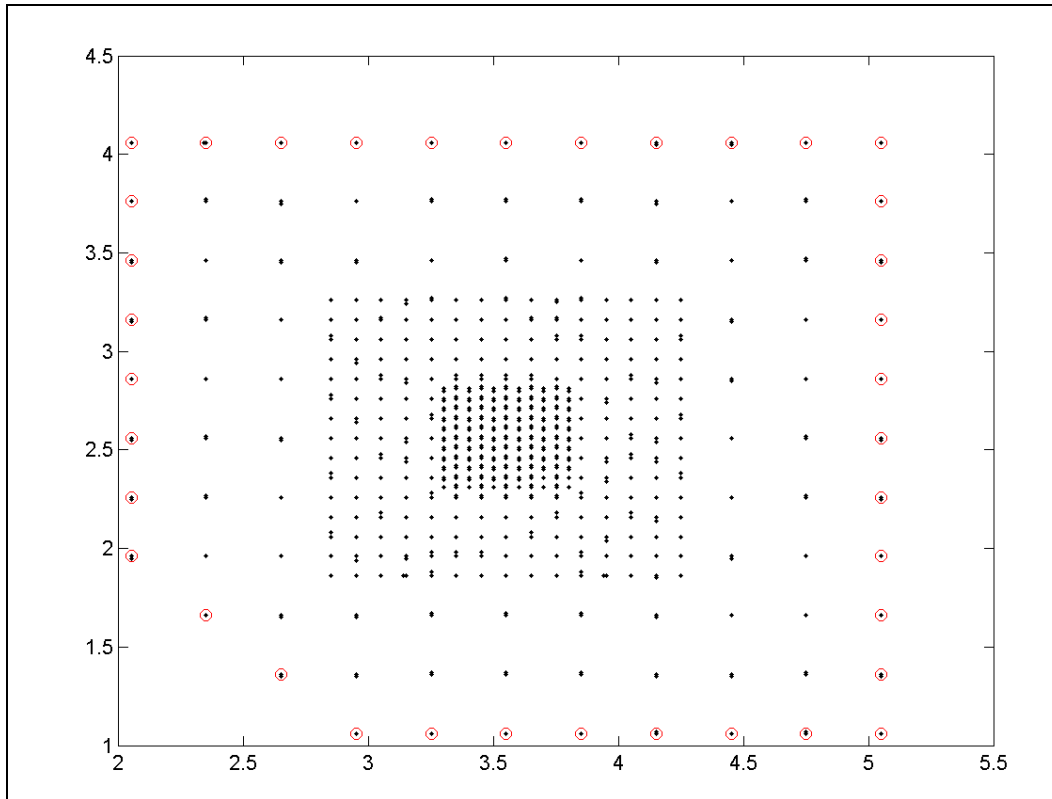
Figure 9. Plan map showing the location of points used in edge leveling. The black dots indicate data points, and the red circles indicate points used in edge drift leveling.
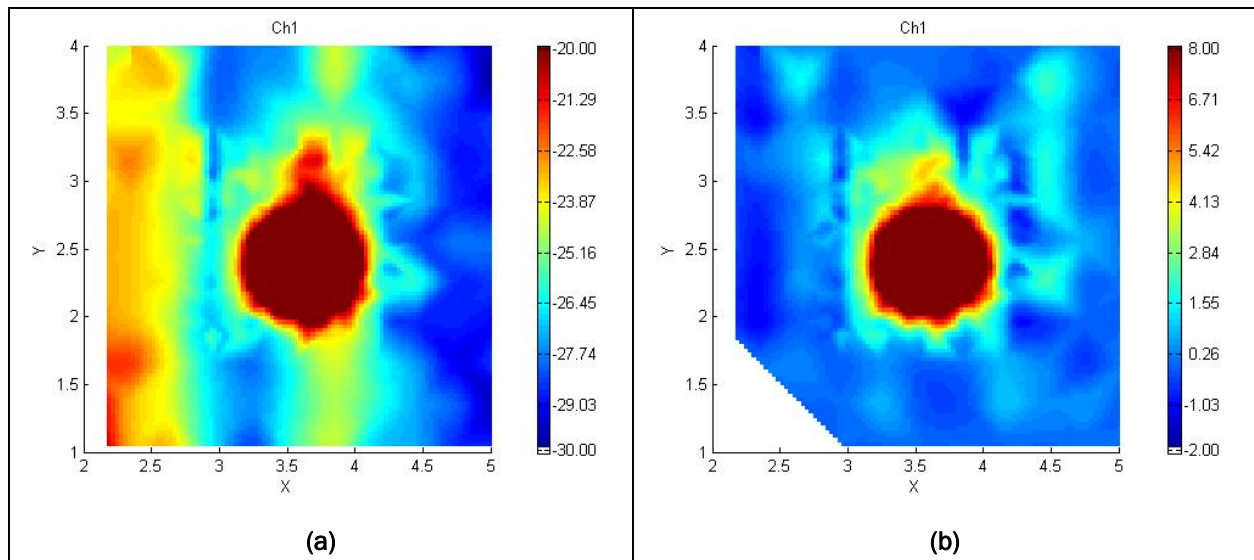
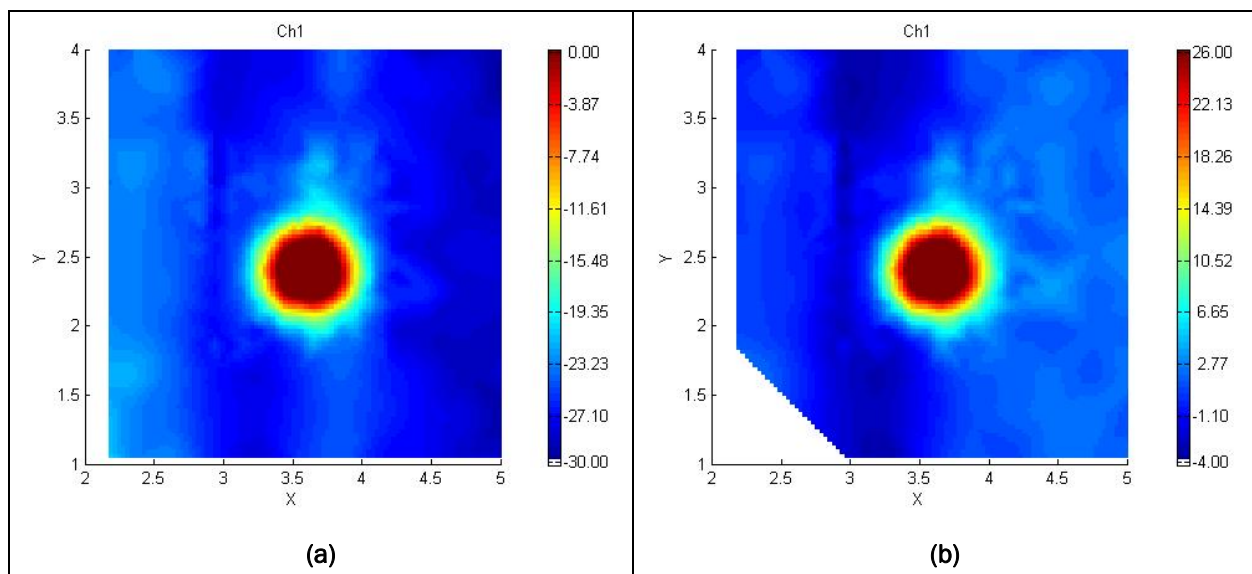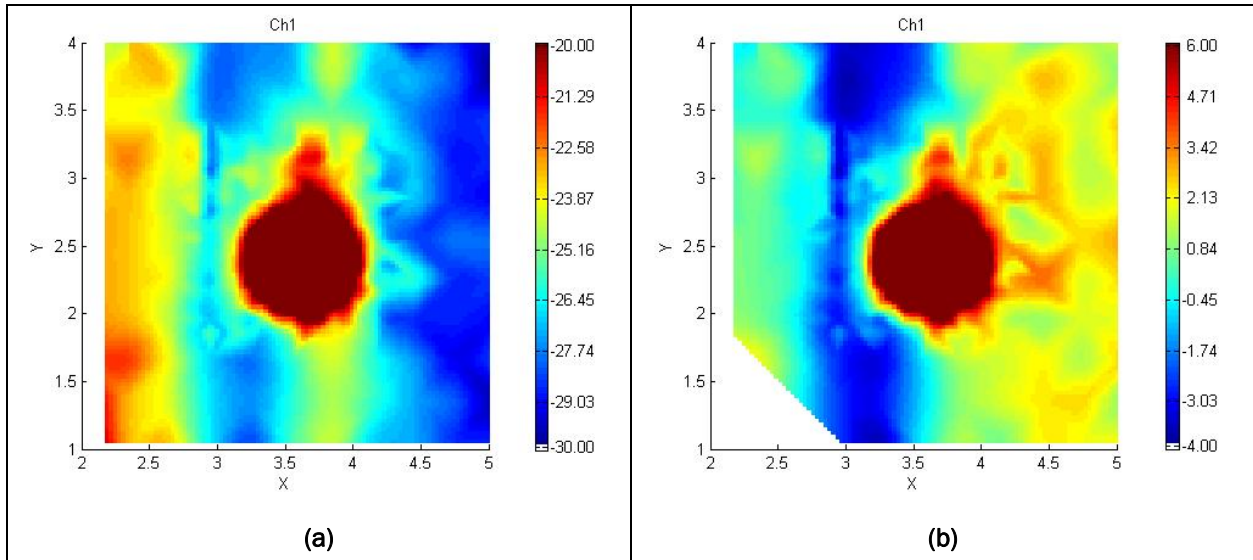Figure 10. Color stretched gridded images of the unleveled (left) and edge-leveled (right) test stand measurements over an ATC 20 mm, depth = 40 cm, dip = 45°, and azimuth = 0°. The color bar in both images has been stretched to include only the lowest 10 mV of data. Panel (a) shows the unleveled data and panel (b) shows the data leveled using the edge measurements from Figure 9. The data are the channel 1 response and the units are millivolts.
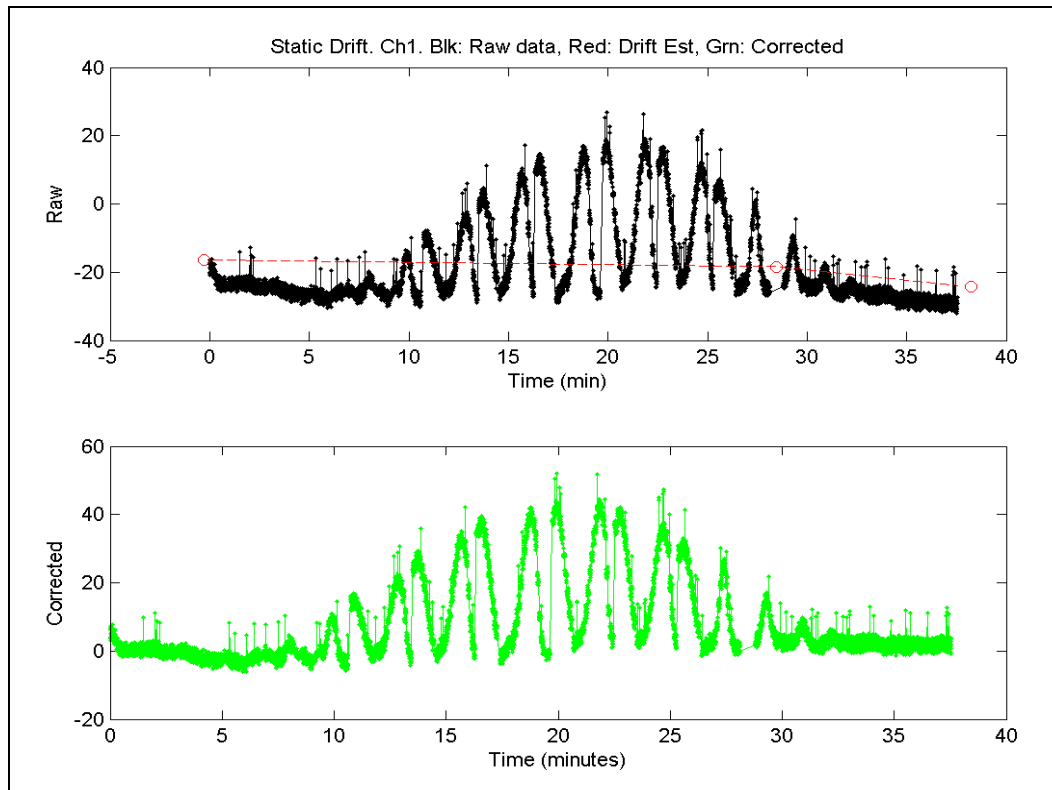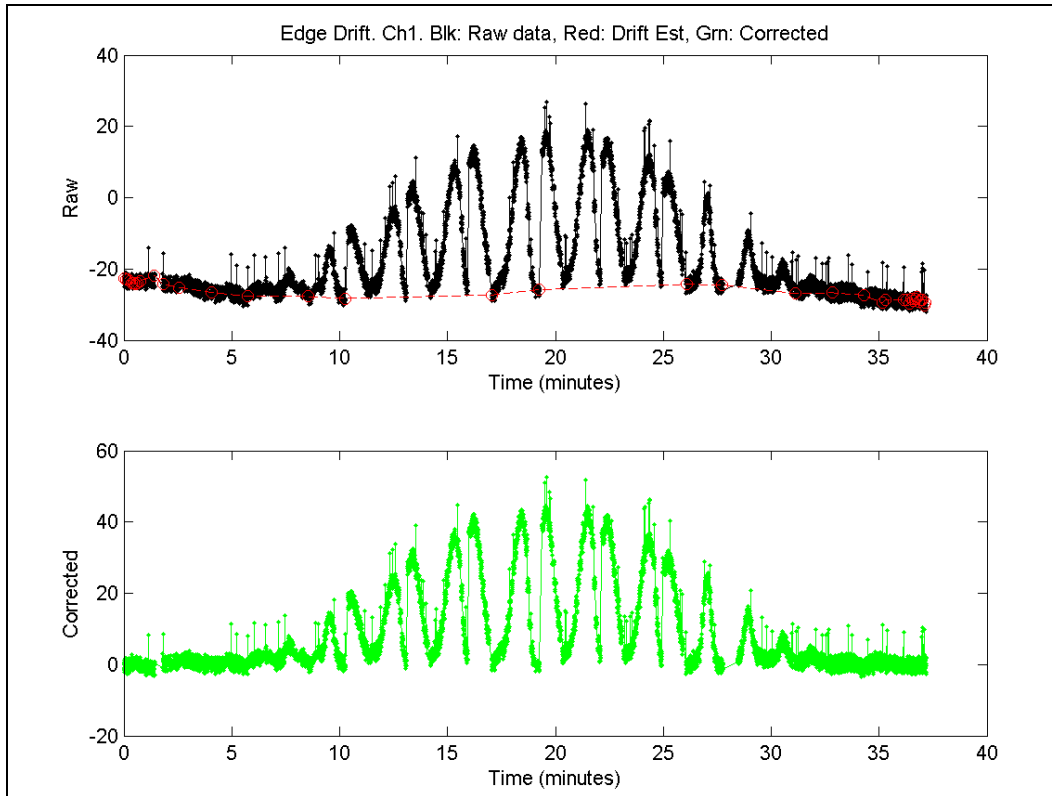
Figure 11. Comparison of unleveled data with edge-leveled data over an ATC 20 mm, depth = 40 cm, dip = 45°, and azimuth = 0°. In the top panel the black profile is the unleveled channel 1 response as a function of time, the red circles represent edge measurements, and the red dotted line is the linearly interpolated values. In the bottom panel, the green profile is the edge-leveled and background corrected response. The channel 1 response is expressed in millivolts and the time is expressed in minutes. Spikes in the data are due to time synch issues within the data; these bad data points are removed during processing.
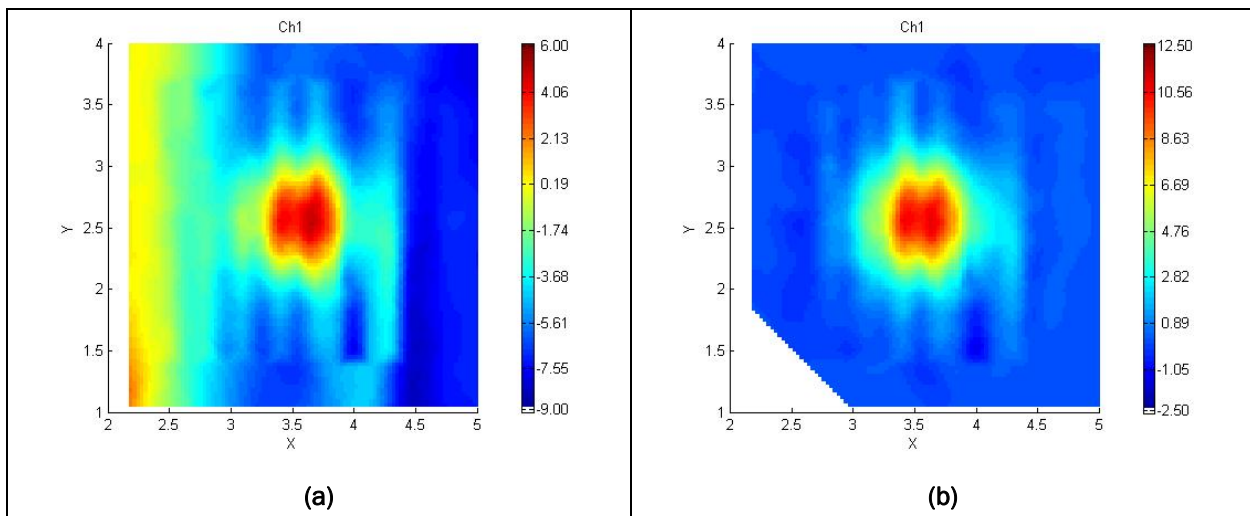
Figure 12. Gridded images of the unleveled (left) and edge-leveled (right) test stand measurements over an ATC 40 mm, depth = 60 cm, dip = -90°, and azimuth = 0°. Panel (a) shows the unleveled data and panel (b) shows the data leveled using the edge measurements from Figure 9. The data are the channel 1 response and the units are millivolts.
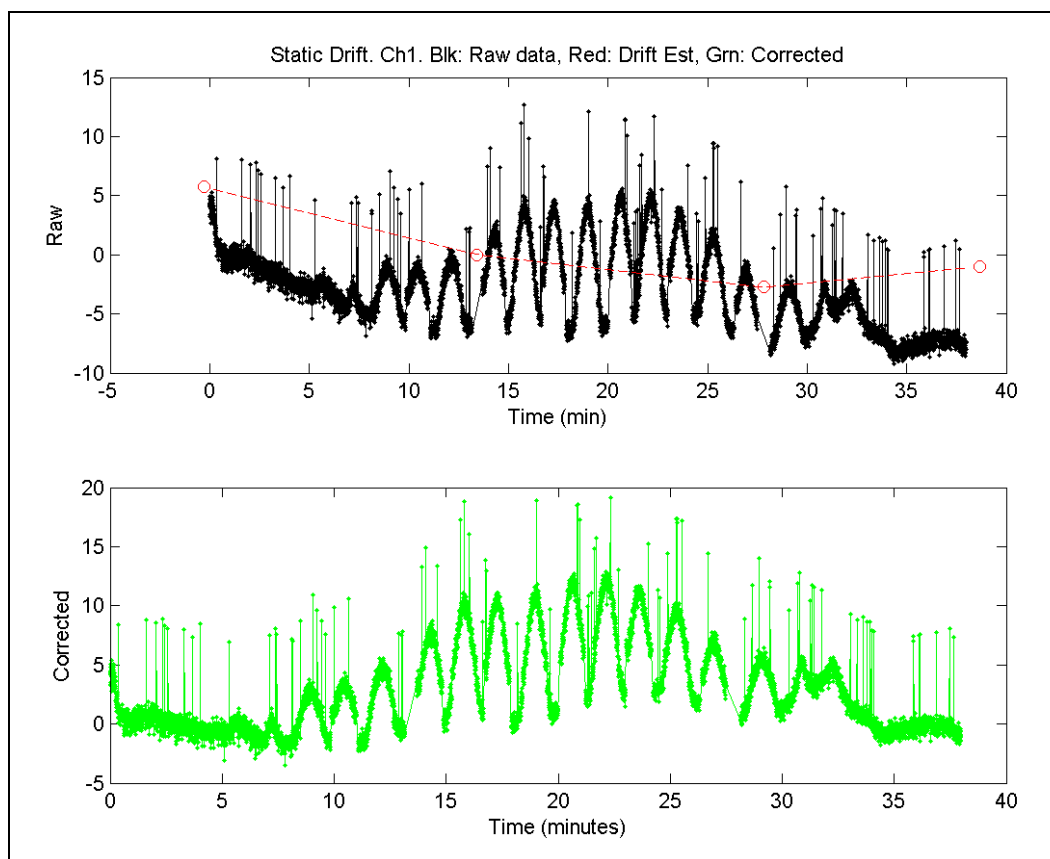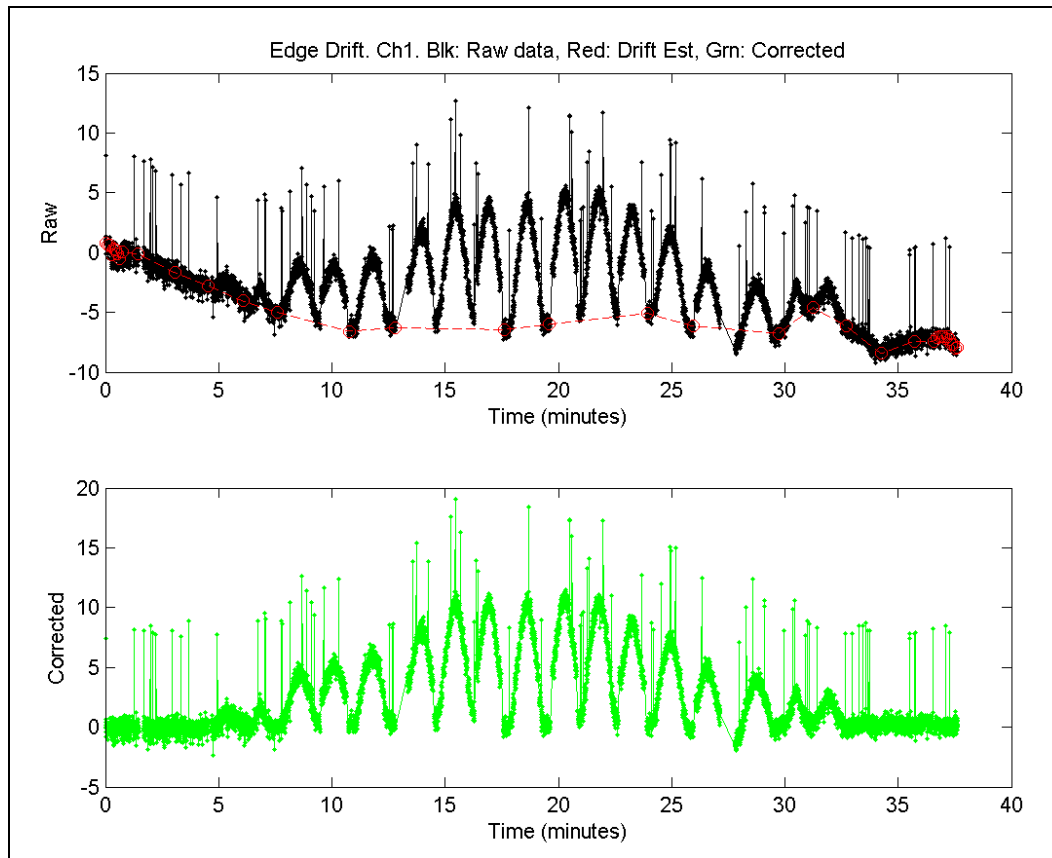
Figure 13. Comparison of unleveled data with edge-leveled data over an ATC 40 mm, depth = 60 cm, dip = -90°, and azimuth = 0°. In the top panel the black profile is the unleveled channel 1 response as a function of time, the red circles represent edge measurements, and the red dotted line is the linearly interpolated values. In the bottom panel, the green profile is the edge-leveled and background corrected response. The channel 1 response is expressed in millivolts and the time is expressed in minutes. Spikes in the data are due to time synch issues within the data; these bad data points are removed during processing.

3.2.2. Frequency domain EM processing

The 2005 GEM-3 data were collected with an incorrect configuration file and a procedure had to be developed to recalibrate the data (see Appendix B). Apart from this fix, the data processing steps applied to the GEM-3 test stand data were fairly standard. The first step was to merge the sensor data with the positional data from the test stand as outlined in the section above. The next step was to apply a background removal and drift correction. No information on the transmitter current is stored in the GEM-3 data. Therefore, the time-based drift correction methodology described in the EM-63 data processing section was used. This methodology was coupled with a background removal based on the assumption that the signal at the edge of the grid was away from any sources. The drift correction worked well in most cases; however, it appears that at certain frequencies

the test stand has a consistent response of its own. Researchers verified that the test stand itself was the source of the patterns in the ordnance survey data by recording survey data with no ordnance present. The background measurement was repeated daily, and the results were very similar each day.

The in-phase and quadrature background data from 90, 510, 3630, and 14070 Hz are shown in Figure 14. The in-phase data contain a linear positive response and a localized negative response that persists in amplitude and spatial extent at all frequencies. The quadrature data are more variable. At 90 Hz the response is on the order of 10 ppm; however, the spatial response was not repeatable from day to day, and the 510-Hz background data were less than 1 ppm and appeared to be random. The 3630- and 14070-Hz data exhibit a pattern similar to the in-phase data; the shape of the response is similar, but the polarity of the response is reversed. The amplitude of the quadrature anomaly increases with frequency. Fortunately, the background response was quite small, relative to the response from the ordnance, and the background response did not have to be removed before fitting dipole models to the data.
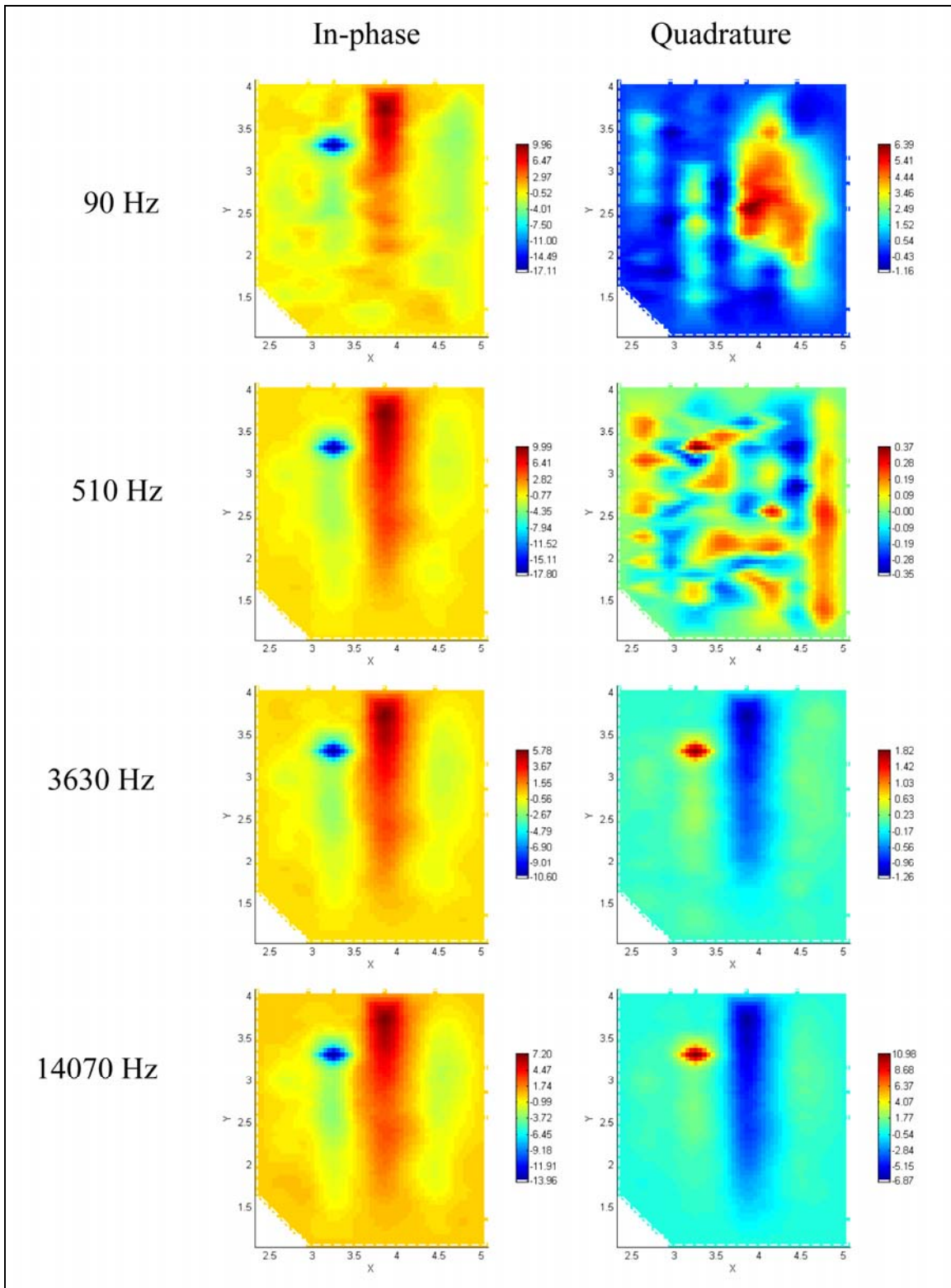
Figure 14. Background GEM-3 response from the test stand. The rows contain gridded images of data at frequencies of 90, 510, 3630, and 14070 Hz (from top to bottom). The left column contains the in-phase data and the right column contains the quadrature data.

4   Images of Data Collected

This chapter provides a summary of the measurements taken over each item by each sensor and presents sample images of the collected data.

4.1. EM-63 data

Table 5 summarizes the EM-63 data collected at the test stand and examples of images of the data over a 20-mm and 155-mm projectile are presented in Figures 15 and 16. The gridded images show how the amplitude diminishes and the shape of the anomaly changes as a function of time. For instance, the horizontal 20-mm projectile has two peaks at early times indicating a substantial horizontal contribution to the induced dipole. The horizontal component becomes even more significant at later times as indicated by the more pronounced separation of the two peaks. The vertical 20-mm projectile has a single peak at all time channels, whereas the 20-mm projectile at 45 degrees has a weak secondary peak that is just discernable at early times. For the horizontal 155-mm projectile (Figure 16), there is a single peak at early times with a transition to a two-peaked anomaly, dominated by the horizontal dipole, at later times.

Table 5. Summary of EM-63 data collection. The "near" measurements were conducted close to the object so that the object response contained a significant contribution non-dipolar component. The "far" measurements were sufficiently far from the object that the secondary field could be modeled as a dipole. All depths are given relative to the center of the object.

Item	Near Dip = 0° Azi = 0°	Near Dip = 45° Azi = 0°	Near Dip = -90° Azi = 0°	Far Dip = 0° Azi = 0°	Far Dip = 45° Azi = 0°	Far Dip = -90° Azi = 0°	Near repeat	Far repeat
ATC 20-mm	z = 0.25 m	z = 0.21 m	z = 0.24 m	z = 0.4 m	z = 0.4 m	z = 0.4 m	Yes	No
ATC 40-mm	z = 0.26 m	z = 0.21 m	z = 0.24 m	z = 0.6 m	z = 0.6 m	z = 0.6 m	Yes	Yes
ATC 60-mm	z = 0.6 m	z = 0.6 m	z = 0.6 m	z = 1.0 m	z = 1.0 m	z = 1.0 m	Yes	No
MN 76-mm	z = 0.6 m	z = 0.6 m	z = 0.6 m	z = 1.0 m	z = 1.0 m	z = 1.0 m	Yes	No
ATC 81-mm	z = 0.6 m	z = 0.6 m	z = 0.6 m	z = 1.0 m	z = 1.0 m	z = 1.0 m	Yes	No
MN 81-mm	z = 0.6 m	z = 0.6 m	z = 0.6 m	z = 1.0 m	z = 1.0 m	z = 1.0 m	Yes	No
MN 90-mm	z = 0.6 m	z = 0.6 m	z = 0.6 m	z = 1.0 m	z = 1.0 m	z = 1.0 m	Yes	No
ATC 105-mm	z = 1.0 m	z = 1.0 m	z = 1.0 m	z=1.5m	z = 1.5 m	z=1.5m	Yes	No
ATC 155-mm	z = 1.0 m	z = 1.0 m	z = 1.0 m	z = 1.5 m	z = 1.5 m	z=1.5m	Yes	No
ATC 2.75-in. Rocket	z = 0.6 m	z = 0.6 m	z = 0.6 m	z = 1.0 m	z = 1.0 m	z = 1.0 m	Yes	No
ATC BDU-28	z = 0.24 m	z = 0.23 m	z = 0.20 m	z = 0.6 m	z = 0.6 m	z = 0.6 m	Yes	No
ATC BLU-26	z = 0.2 m	z = 0.21 m	z = 0.21 m	z = 0.6 m	z = 0.6 m	z = 0.6 m	Yes	No
ATC M42	z = 0.25 m	z = 0.25 m	z = 0.25 m	z = 0.6 m	z = 0.6 m	z = 0.6 m	Yes	No

Item	Near Dip = 0° Azi = 0°	Near Dip = 45° Azi = 0°	Near Dip = -90° Azi = 0°	Far Dip = 0° Azi = 0°	Far Dip = 45° Azi = 0°	Far Dip = -90° Azi = 0°	Near repeat	Far repeat
ATC MK118	z = 0.25 m	No	No	z = 0.6 m	z = 0.6 m	z = 0.6 m	No	Yes
MN Frag1	z = 0.6 m	z = 0.6 m	z = 0.6 m	No	No	No	Yes	No
MN Frag2	z = 0.6 m	z = 0.6 m	z = 0.6 m	No	No	No	Yes	No
MN Frag3	z = 0.6 m	z = 0.6 m	z = 0.6 m	No	No	No	Yes	No
HSL Cylinder	z = 0.6 m	z = 0.6 m	z = 0.6 m	z = 0.75 m	No	No	Yes	No
HSS Cylinder	z = 0.6 m	z = 0.6 m	z = 0.6 m	z=0.75m	No	No	Yes	No
SAL Cylinder	z = 0.6 m	z = 0.6 m	z = 0.6 m	z=0.75m	No	No	Yes	No
SAS Cylinder	z = 0.6 m	z = 0.6 m	z = 0.6 m	z = 0.75 m	No	No	Yes	No
SSL Cylinder	z = 0.6 m	z = 0.6 m	z = 0.6 m	z = 0.75 m	No	No	Yes	No
SSS Cylinder	z = 0.6 m	z = 0.6 m	z = 0.6 m	z = 0.75 m	No	No	Yes	No

4.2. EM-61 data

Table 6 summarizes the EM-61 data collected at the test stand and Figure 17 shows some examples of leveled data.

4.3. GEM-3 data

Table 7 summarizes the GEM-3 data collected at the test stand, and example images of the data are presented in Figures 18 and 19.

The gridded images show that not only the amplitude and polarity of the in-phase and quadrature response varies with frequency, but the spatial extent of the anomaly also changes. In the top right panel of Figure 18, the 90-Hz quadrature response is approximately 60 ppm and has an elongated shape with two peaks. As the frequency increases, the response becomes spatially more compact and the amplitude increases to a maximum around 1000 Hz. As the frequency continues to increase, the amplitude decreases but the size of the anomaly remains constant. The frequency spectra plotted in Figure 19 show the in-phase and quadrature response directly above a Montana 90-mm projectile for three orientations at two depths.

As the orientation of the ordnance varies, the character of the in-phase and quadrature curves vary; and as the depth of the ordnance increases, the amplitudes of the anomalies decrease. The combination of the spectral information contained in individual soundings and the spatial information

provided by full coverage grids is invaluable in discriminating the response of various targets at various orientations and depths.
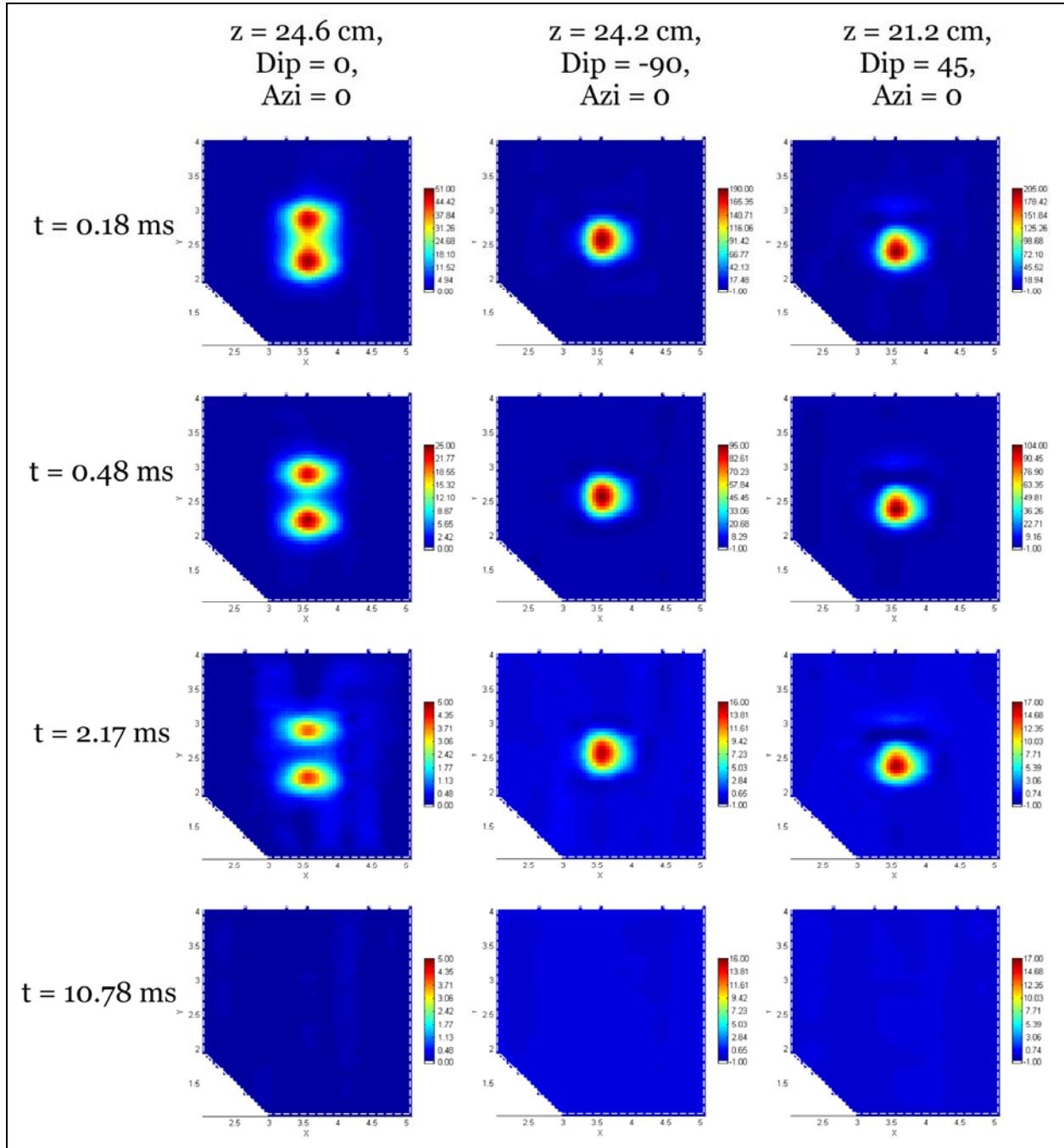
Figure 15. ATC 20-mm data plots.
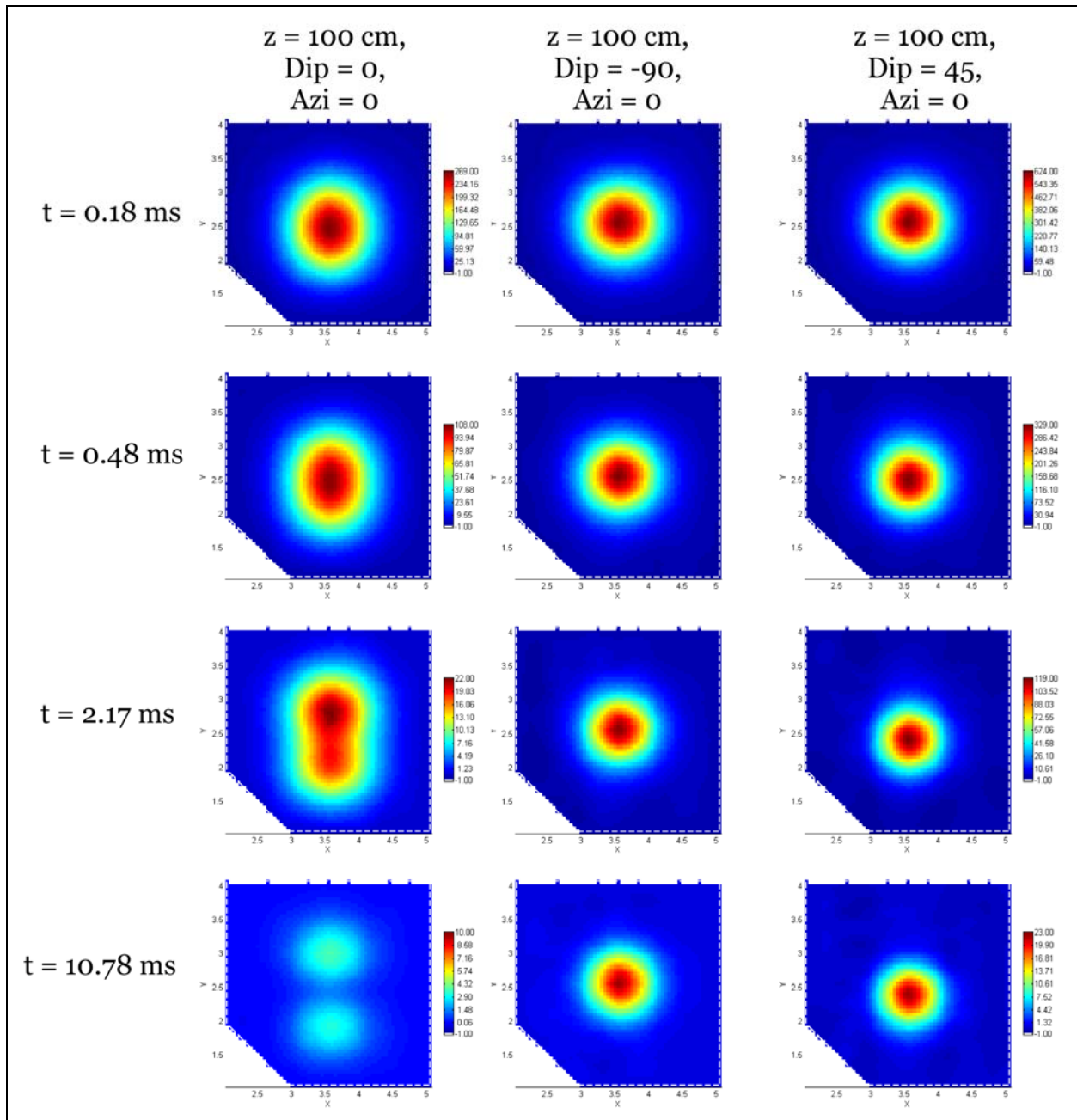
Figure 16. ATC 155-mm data plots.

Table 6. List of ordnance measured with the EM-61.

Item	Near, Dip = 0°, Azi = 0°	Near, Dip = 45°, Azi = 0°	Near, Dip = -90°, Azi = 0°	Far, Dip = 45°, Azi = 0°
50-caliber bullet	z = 20 cm	z = 20 cm	z = 20 cm	z = 30 cm
20-mm (ATC)	z = 20 cm	z = 20 cm	z = 20 cm	z = 30 cm
20-mm (FLBGR)	z = 20 cm	z = 20 cm	z = 20 cm	z = 30 cm
37-mm	z = 40 cm	z = 40 cm	z = 40 cm	z = 60 cm
60-mm mortar	z = 60 cm	z = 60 cm	z = 60 cm	z = 100 cm

Figure 17. Example images of EM-61 data collected at the test stand. The left column shows time-channel 1 data; the right column, time channel 4. From top to bottom, the images are 50-caliber bullet, 20-mm ATC projectile, 37-mm projectile, and 60-mm mortar. In each case, the ordnance was at a dip of 45 degrees and an azimuth of 0 degrees.

Table 7. List of ordnance measured with the GEM-3.

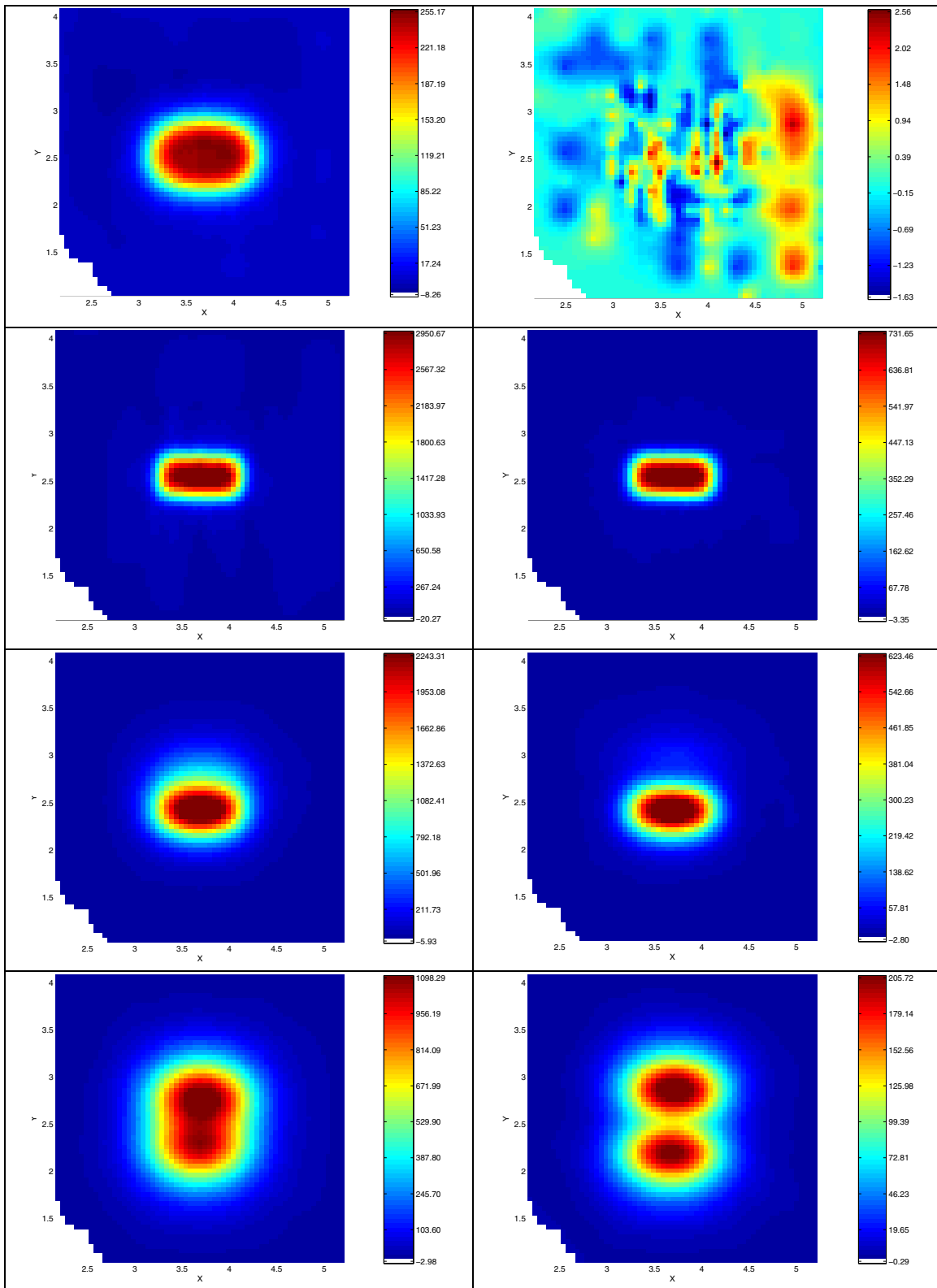| Item	Near, Dip = 0° Azi = 0°	Near, Dip = 45° Azi = 0°	Near Dip = -90° Azi = 0°	Far Dip = 0° Azi = 0°	Far Dip = 45° Azi = 0°	Far Dip = -90° Azi = 0°	Near repeat	Far repeat
2005								
ATC 37-mm	z = 0.3 m	z = 0.3 m	z = 0.3 m	z = 0.4 m	z = 0.4 m	z = 0.4 m	No	Yes
MN 76-mm	z = 0.5 m	z = 0.5 m	z = 0.5 m	z = 0.75 m	z = 0.75 m	z = 0.75 m	Yes	No
MN 81-mm	z = 0.5 m	z = 0.5 m	z = 0.5 m	z = 0.75 m	z=0.75m	z = 0.75 m	Yes	No
MN 90-mm	z = 0.5 m	z = 0.5 m	z = 0.5 m	z = 0.75 m	z=0.75m	z = 0.75 m	Yes	No
HSL Cylinder	z = 0.5 m	z = 0.5 m	z = 0.5 m	z = 0.75 m	No	No	No	No
HSS Cylinder	z = 0.5 m	z = 0.5 m	z = 0.5 m	z = 0.75 m	No	No	No	No
SAL Cylinder	z = 0.5 m	z = 0.5 m	z = 0.5 m	z = 0.75 m	No	No	No	No
SAS Cylinder	z = 0.5 m	z = 0.5 m	z = 0.5 m	z = 0.75 m	No	No	No	No
SSL Cylinder	z = 0.5 m	z = 0.5 m	z = 0.5 m	z = 0.75 m	No	No	No	No
SSS Cylinder	z = 0.5 m	z = 0.5 m	z = 0.5 m	z = 0.75 m	No	No	No	No
2006								
ATC 20-mm	z = 0.2 m	z = 0.2 m	z=0.2	No	z = 0.3 m	No	No	No
ATC 37-mm	No	z = 0.3 m	No	z = 0.4 m	z = 0.4 m	z = 0.4 m	No	No
ATC 40-mm	z = 0.3 m	z = 0.3 m	z = 0.3 m	No	z = 0.4 m	No	No	No
ATC 60-mm	z = 0.4 m	z = 0.4 m	z = 0.4 m	No	z = 0.5 m	No	No	No
ATC BLU-26	z = 0.2 m	z = 0.2 m	z = 0.2 m	No	z = 0.3 m	No	No	No
ATC 81-mm	z = 0.5 m	z = 0.5 m	z = 0.5 m	No	z = 0.7 m	No	No	No
ATC 2.75-in.	z = 0.5 m	z = 0.5 m	z = 0.5 m	No	z = 0.7 m	No	No	No
ATC 105-mm	z = 0.6 m	z = 0.6 m	z = 0.6 m	No	z = 0.8 m	No	No	No
ATC 155-mm	z = 0.7 m	z = 0.7 m	z = 0.7 m	No	z = 1.0 m	No	No	No
ATC M42	z = 0.2 m	z = 0.2 m	z = 0.2 m	No	z = 0.3 m	No	No	No
ATC MK118	z = 0.2 m	z = 0.255 m	z = 0.2 m	No	z = 0.3 m	No	No	No
ATC BDU-28	z = 0.2 m	z = 0.2 m	z = 0.2 m	No	z = 0.3 m	No	No	No
50-caliber	z = 0.2 m	z = 0.2 m	z = 0.2 m	No	z = 0.3 m	No	No	No
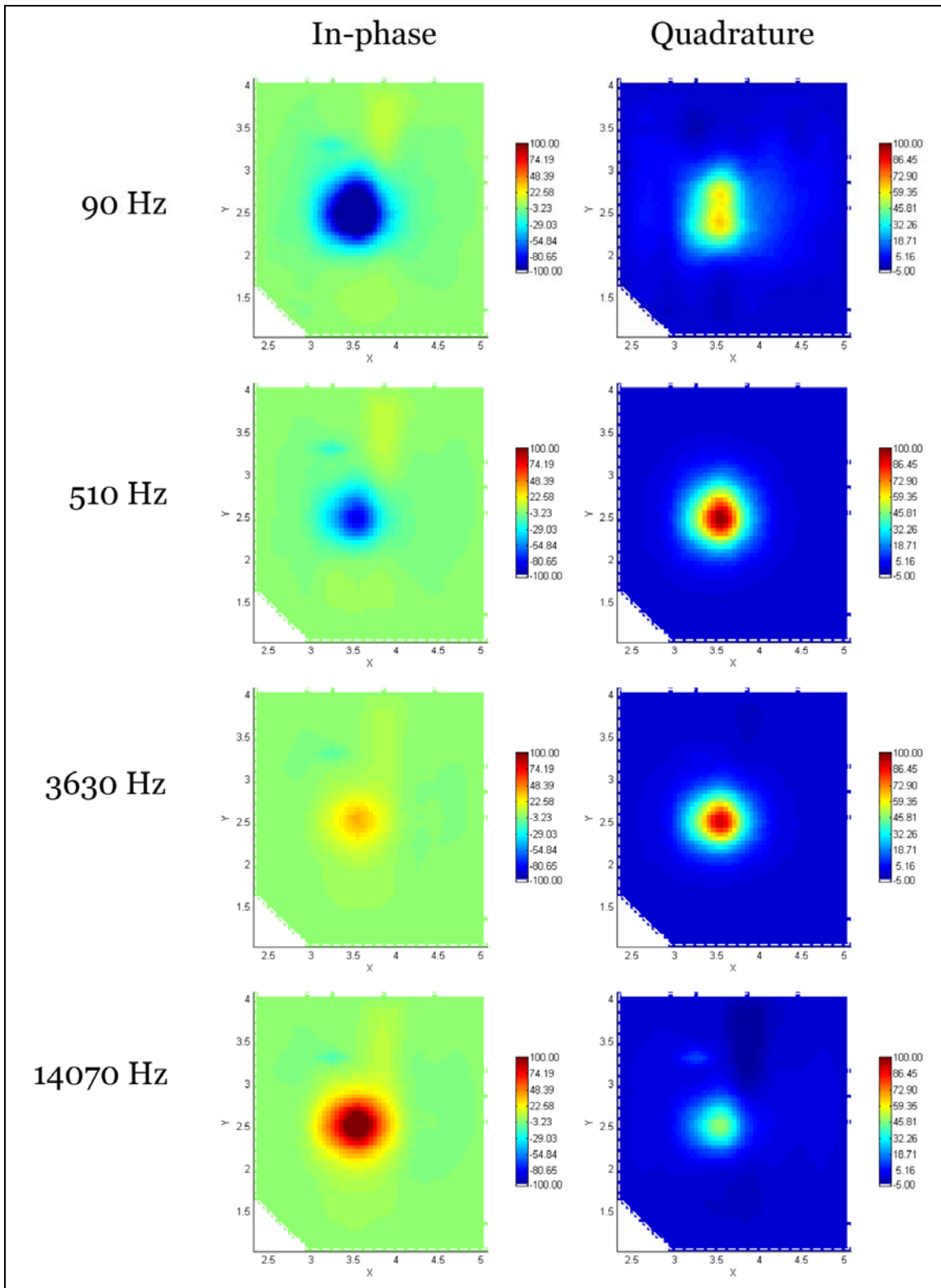
Figure 18. Summary of GEM-3 measurements over the Montana 90-mm projectile at depth = 50 cm, dip = 0°, azimuth = 0°. The rows contain gridded images of data at frequencies of 90, 510, 3630, and 14070 Hz (from top to bottom). The left column contains the in-phase data and the right column contains the quadrature data.
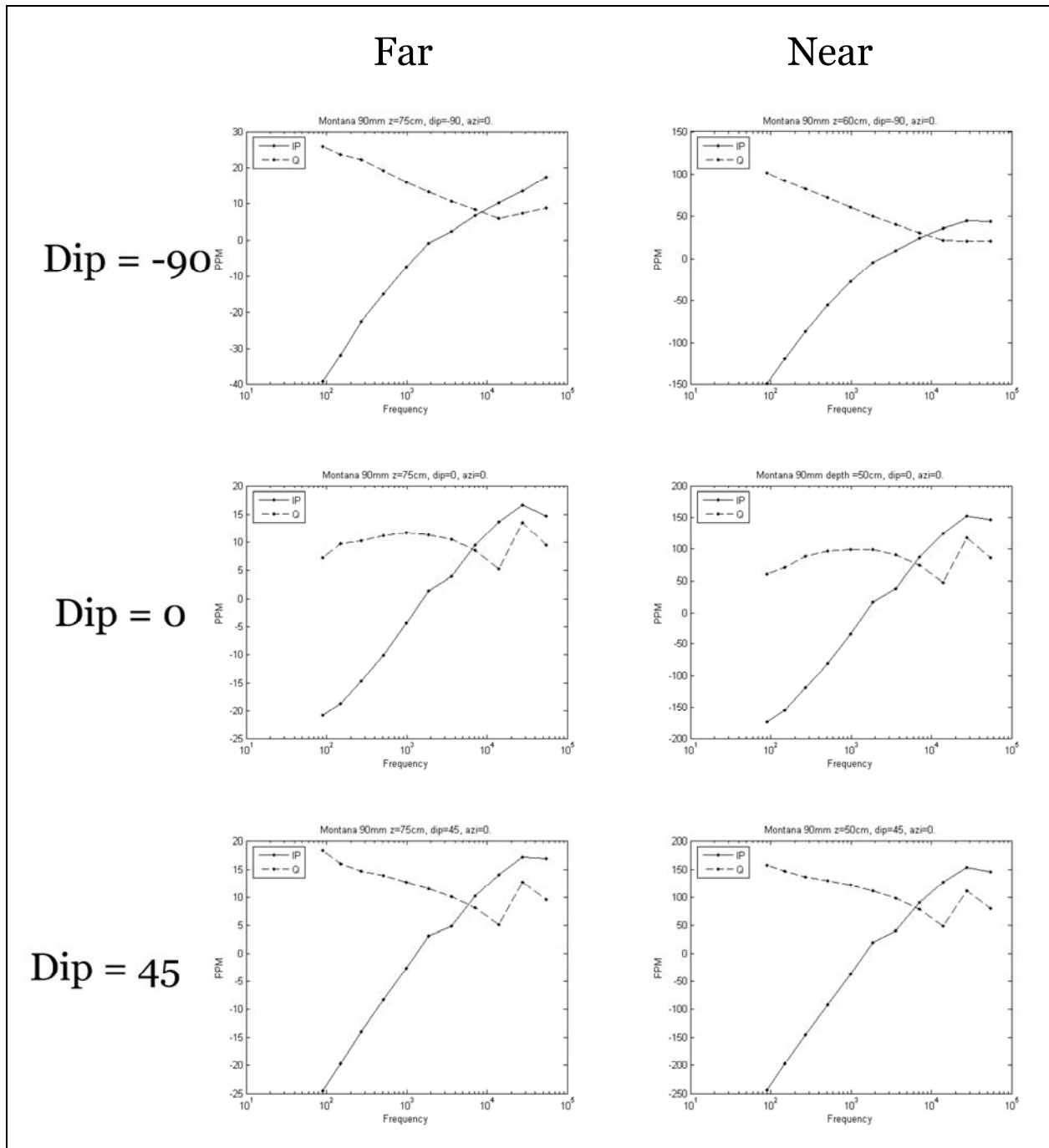
Figure 19. GEM-3 frequency spectra from a Montana 90-mm projectile. The in-phase and quadrature components are plotted directly above the target for three orientations at two depths. The left column shows the spectrum at 75-cm depth and the right column shows it at 50-cm depth.

5 Dipole Model Fits to EM-63, EM-61, and GEM-3 Data

This chapter describes the dipole fitting that was used to model each of the ordnance items measured with the EM-61, EM-63, and GEM-3. Also identified are the parameters of the dipole models that have the potential to be used for discrimination.

5.1. Inversion of EM-63 data

The Geonics EM-63 data collected over each of the 14 ordnance items and three calibration cylinders were inverted for best fit polarization tensors. The *kbg* version of the Pasion-Oldenburg (P-O) formulation (Pasion and Oldenburg 2001; and Report 6), which does not involve an early time alpha parameter,

$$L_i(t) = k_i \, t^{-\beta_i} \exp(-t / \gamma_i) \tag{1}$$

for i = {1, 2, 3} and with the constraint that $L_2(t) = L_3(t)$. One of the objectives of these inversions was to accurately determine the polarization tensor for each target. In order to reduce the trade-off between polarization parameters and the depth/location/orientation, the orientation was constrained to within ±5 degrees of the true value and the depth was constrained to within 2 cm. These results will:

1. Provide information on the spread of polarization parameters for different orientations of a given object (in theory, the polarization parameters are an invariant property of the object);
2. Determine the class separation between various UXO items in parameter space; and
3. Help in assessing the effectiveness of the inversion techniques when applied to test plot data (since these targets are being buried in the Ashland test plot, and these accurately determined polarization tensors would serve as ground truth).

Figure 20 contains a sample fit applied for data collected over the short, hollow, steel calibration cylinder, while Figure 21 plots the axial and transverse polarization components for all the calibration cylinders. The

differences in permeability, conductivity, shape, and whether the cylinder is solid or hollow, are reflected in the best polarization components. In addition to being calibration data, these cylinder data will be used to test and evaluate more numerically rigorous electromagnetic modeling (see Report 6). Figure 22 shows the polarization tensors for the ATC 40-mm and the ATC 81-mm targets for a number of orientations and depths.

During the polarization tensor analysis, it was established that the dipole model can accurately model the different data sets. The extracted polarization tensor parameters are similar for different orientations and depths, suggesting that each target can be modeled by a single polarization tensor. The 20-mm target data do not model well with a single polarization tensor; this is likely due to the target's close proximity to the EM-63 (<30 cm from the transmitter loop) during the measurements.

Figure 23 shows how the different targets separate within the (k_1, k_2) feature space. Each target is well grouped in this space, with some overlap particularly for the medium caliber projectiles. If the dipole model exactly described the response of each UXO, and if the data could constrain each inversion parameter, then each cluster would collapse to a single point in parameter space.

Figure 24 shows plots of the other polarization tensor parameters extracted from the test stand data, including primary and secondary betas and gammas. For these inversions the constraints were relaxed on the dipole position and the constraints on orientation were completely removed (so that the inversion results are more representative of what could be obtained if there were no prior information on the target). There is some spread in the parameter clusters, but the decay characteristics of the polarization tensors are relatively distinct between the ordnance types. In Figures 24c and 24d, the size of the primary and secondary polarizations at time channel 1 are plotted versus the relative decay of the polarization (computed as the ratio of the polarization at time channel 20 over that at time channel 1).

(a) Observed Data (*t* = 0.18 ms)

(b) Predicted Data (*t* = 0.18 ms)

(c) Residual (*t* = 0.18 ms)

(d) Decay fit directly over target
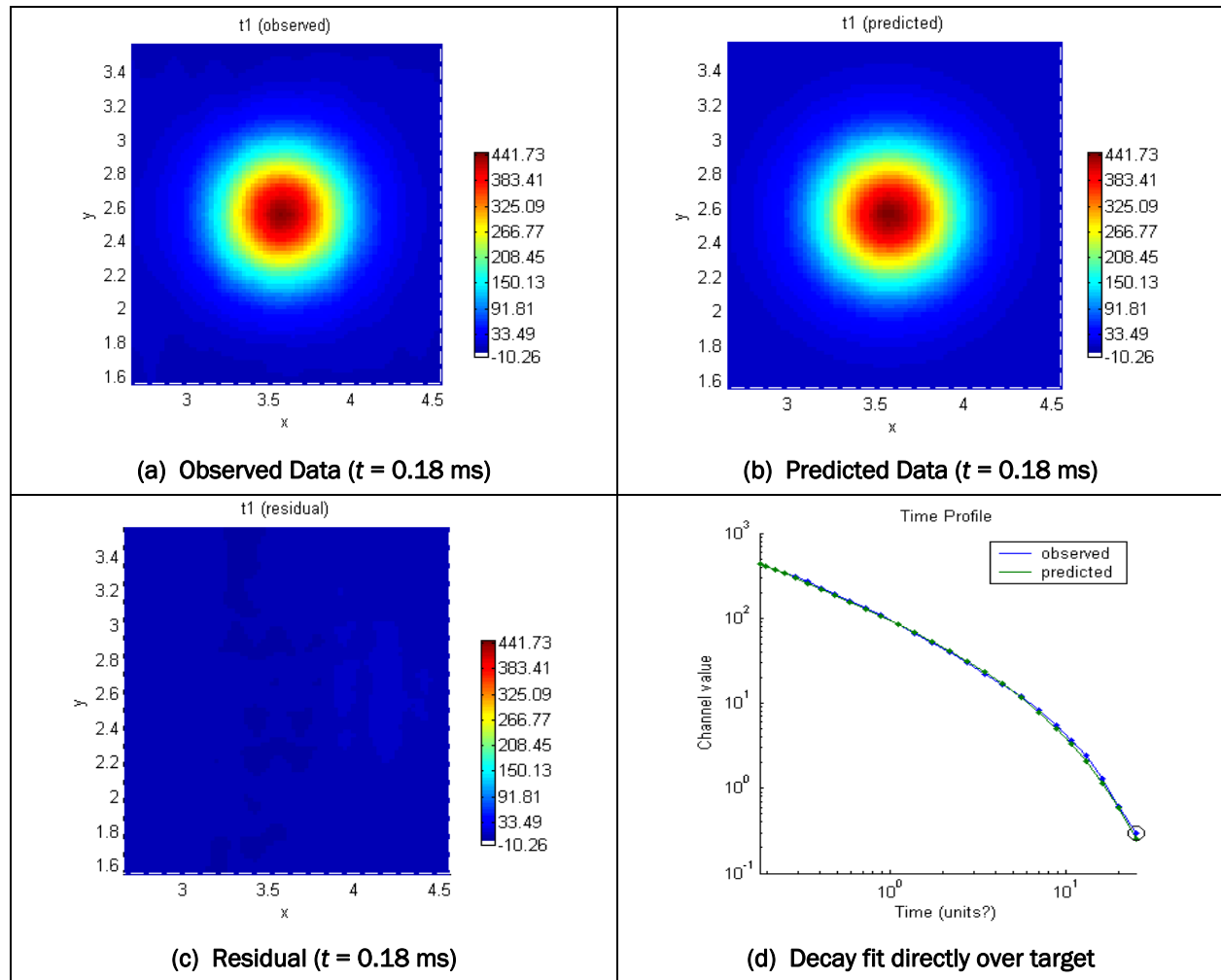
Figure 20. Fitting results for the short hollow steel calibration cylinder.

(a) Axial Polarization

(b) Transverse Polarization
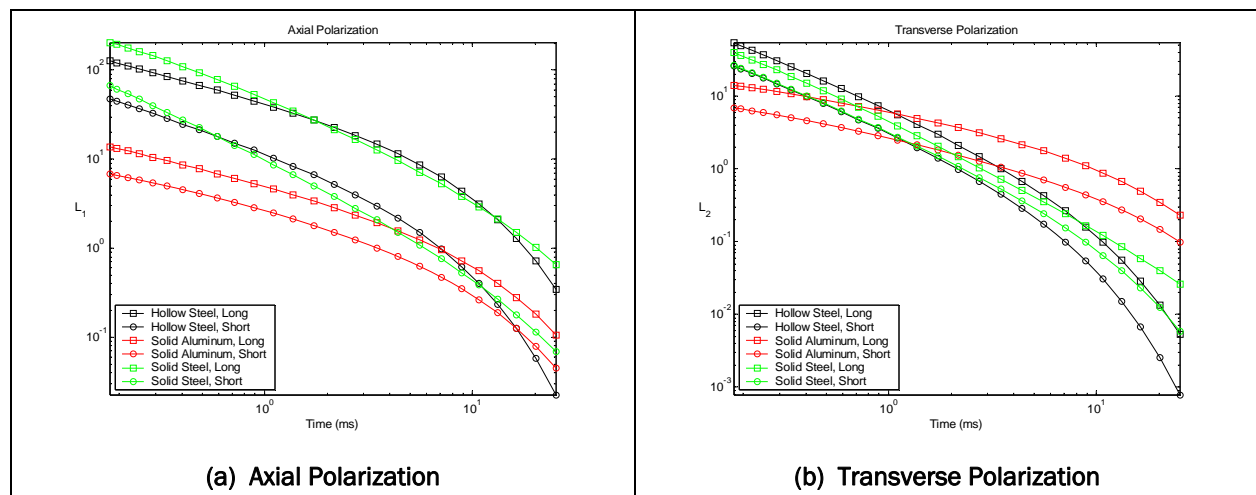
Figure 21. Axial and transverse polarizations for steel and aluminum calibration cylinders. The hollow steel cylinder has a faster power law decay and shorter time constant than its solid counterpart. The hollow steel cylinder behaves like a solid cylinder with a lower permeability.
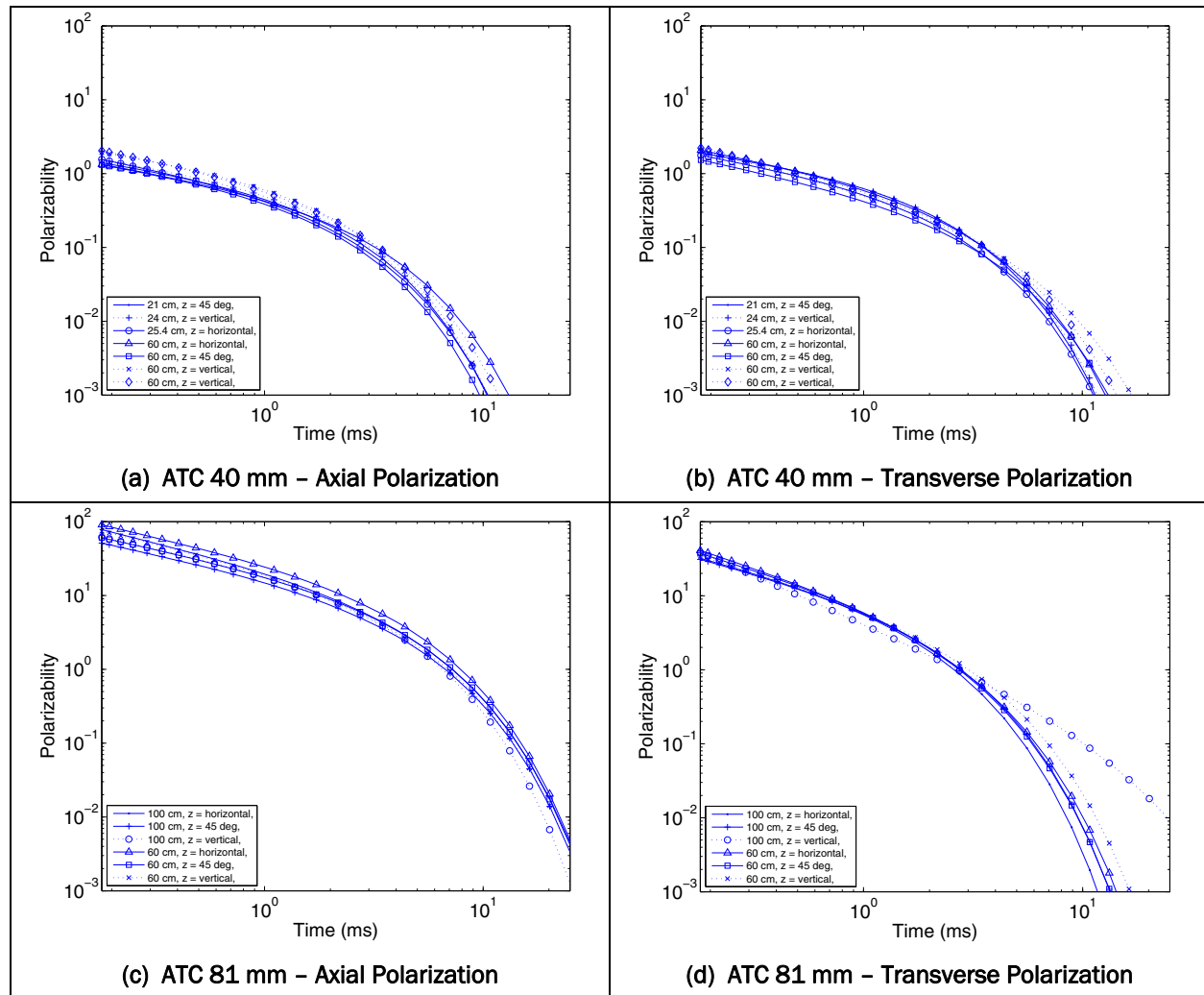
Figure 22. Recovered polarizations for Aberdeen Test Center 40-mm and 81-mm targets. In panel (d) a deeper vertical target has a poorly constrained transverse polarization due to the EM-63 transmitter being primarily in the vertical direction and the lower signal-to-noise ratio at a distance of 100 cm from the transmitter loop.

For the primary polarizations, most of the decay ratios are around 0.01, with the primary polarization falling off much faster for the BLU-26 and M42 (ratio = 0.00001). Presumably this is due to the thin and/or aluminum walls in the BLU-26 and M42. For the secondary polarizations the results are similar, although the parameter values show greater spread (it is unlikely that the secondary polarization will be resolved to the same degree of precision as the primary polarization). The main implication of these results is that relative decay rates can provide some information on ordnance type. However, of perhaps more significance, the spread of values for a wide range of ordnance types is fairly limited. This means that
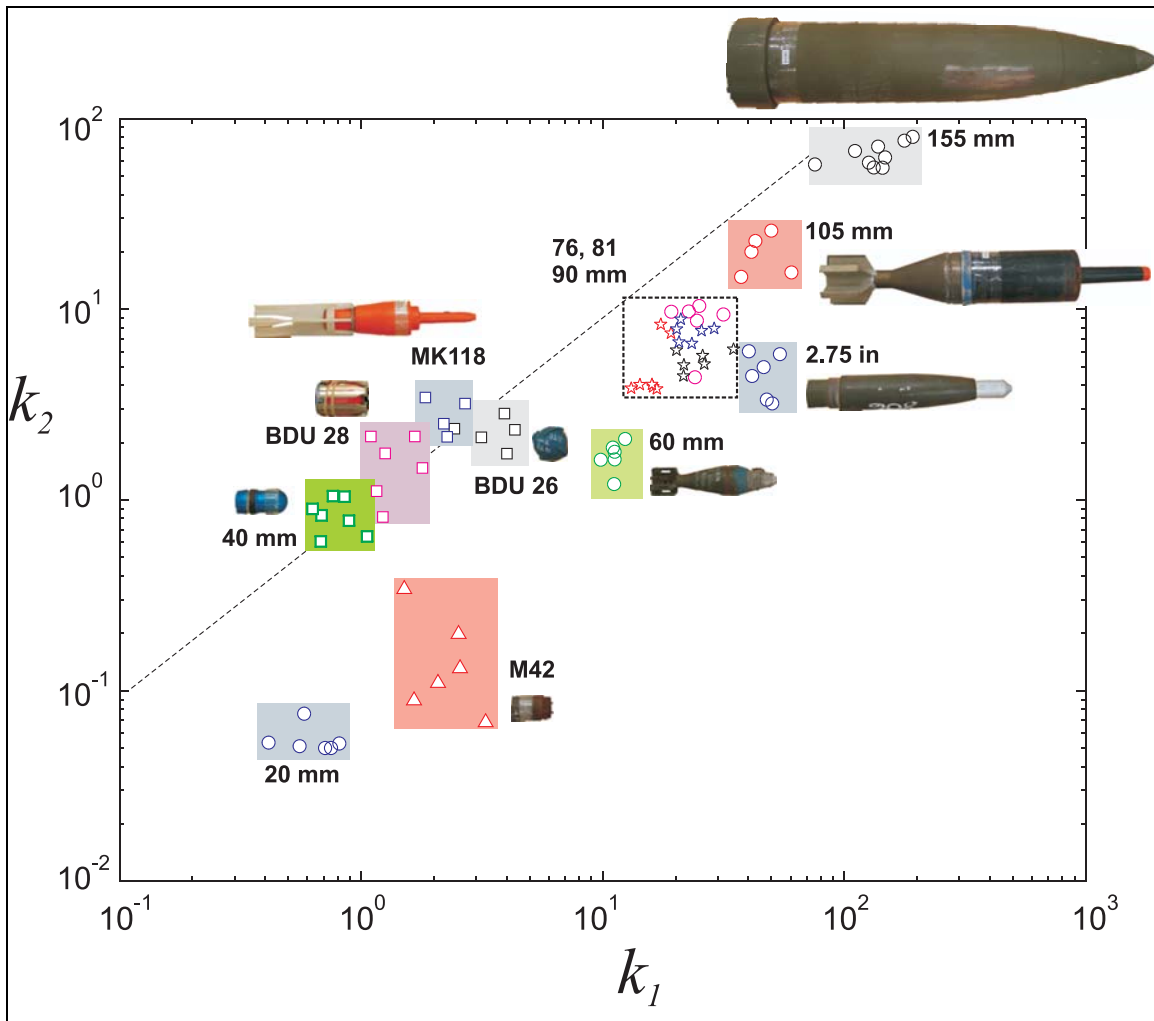
Figure 23. k-parameter plot demonstrating the clustering according to ordnance type. Note that the 20-mm class is tightly clustered, even though the data fits to some of the items were relatively poor.

the relative decay rate could be highly diagnostic of UXO potential: items such as thin-walled scrap and shrapnel will likely have faster decay rates and, hence, could be distinguished from UXO. Of course, this task would be more challenging if BLU-26 or M42 munitions are present on the site.
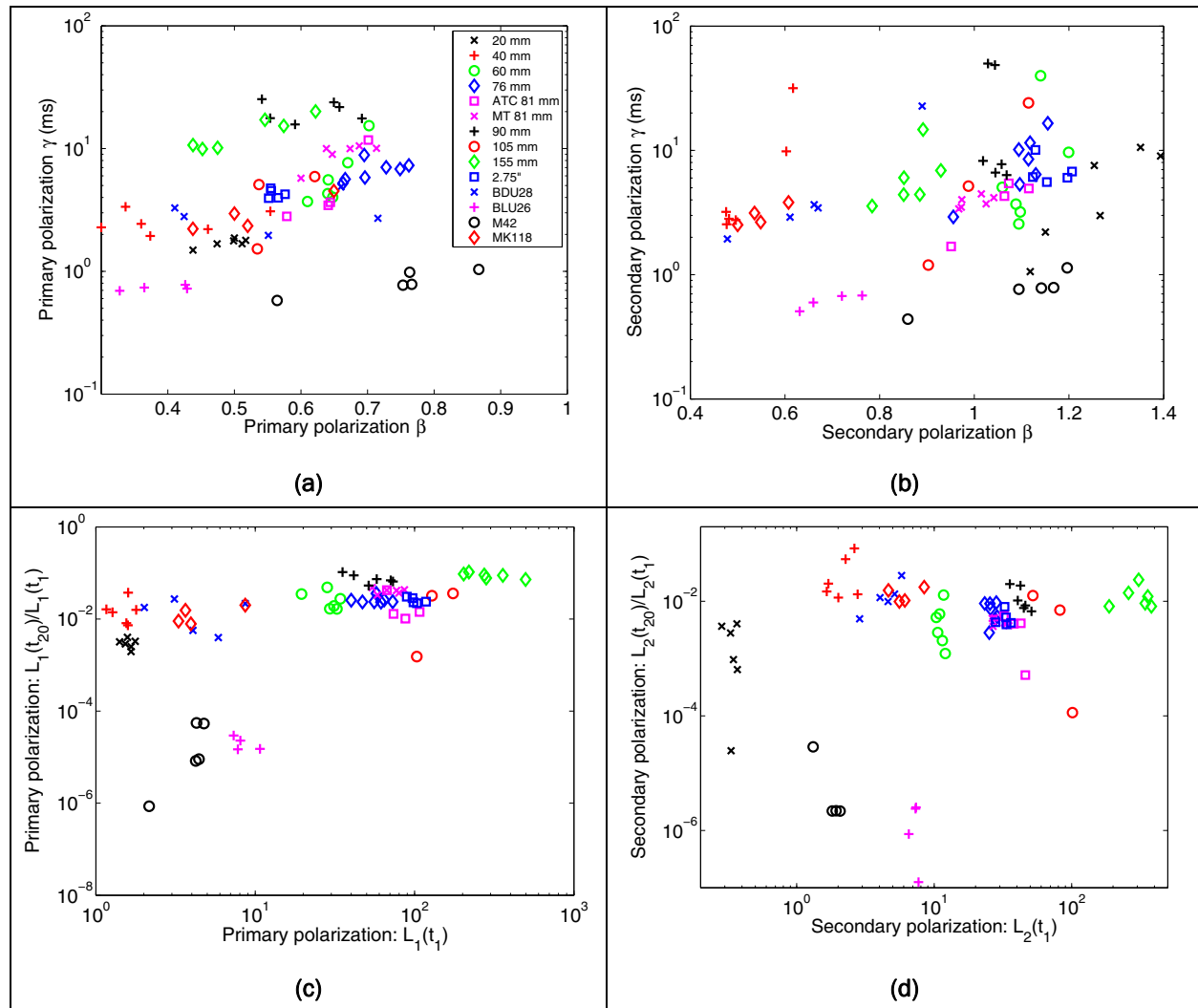
Figure 24. Recovered Pasion-Oldenburg models for EM-63 data on the test stand: (a) Plots primary β versus primary γ; (b) Plots secondary β versus secondary γ; (c) plots the primary polarization at time channel 1 versus the relative decay (from time channel 1 to 20) of the primary polarization; and (d) same as for (c) but for the secondary polarization.

5.2. Inversion of EM-61 data

Five types of ordnance were measured on the test stand using the EM-61: 50-caliber bullets; two types of 20-mm projectiles (ATC and Former Lowry Bombing and Gunnery Range (FLBGR)); a 37-mm projectile; and the 60-mm mortar. The ability to distinguish hazardous 37-mm projectiles from less hazardous 20-mm projectiles and 50-caliber bullets was the discrimination goal for the work performed at the 20-mm Range Fan at FLBGR. To determine which features might be diagnostic between the different items, two-dipole instantaneous amplitude models[1] were

---

[1] Otherwise referred to as a beta-model (Bell et al. 2001).

recovered for each of the four sets of measurements made on each item. Figures 25 and 26 provide an example of the recovered dipole fit at time channels 1 and 4 to a horizontal 60-mm mortar, 60 cm below the EM-61. There is very close agreement between the measured data and the dipole model, with the residuals typically less than 5 percent of the data values. Fits to the other EM-61 test stand data are of comparable quality.

Figure 27 plots the instantaneous amplitude parameters recovered from inversion of all the EM-61 test stand data. The amplitude of $L_1(t_1)$ or $L_2(t_1)$ is an effective discriminator between the 50-caliber bullets, 20-mm and 37-mm projectiles, and the 60-mm mortar. The amplitudes for both types of 20-mm projectile are similar. The 50-caliber bullets exhibit a much more rapid decay in amplitude with time than do the other projectiles.
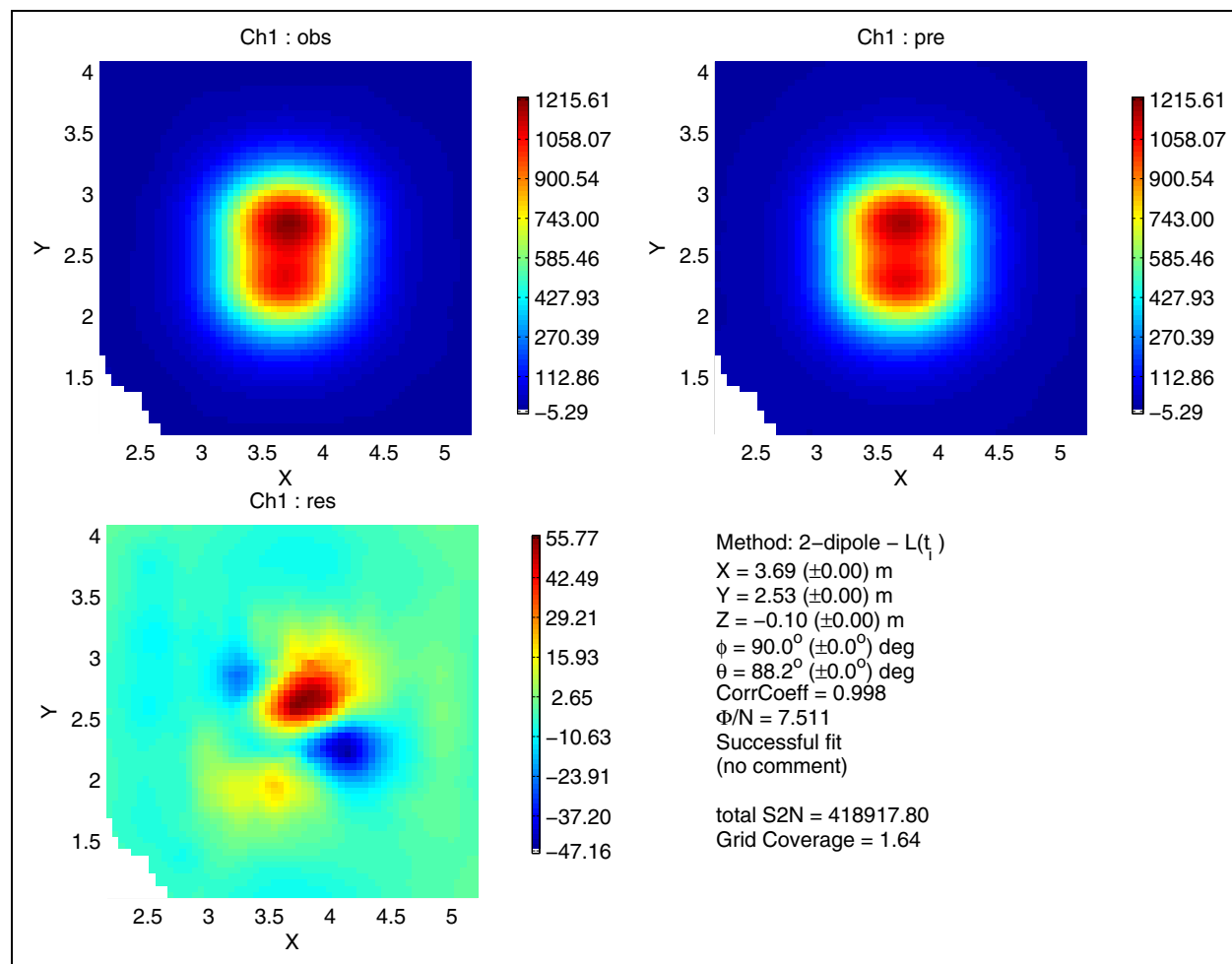
Figure 25. Two-dipole fit at time channel 1 to a horizontal 60-mm mortar 60 cm below the EM-61.
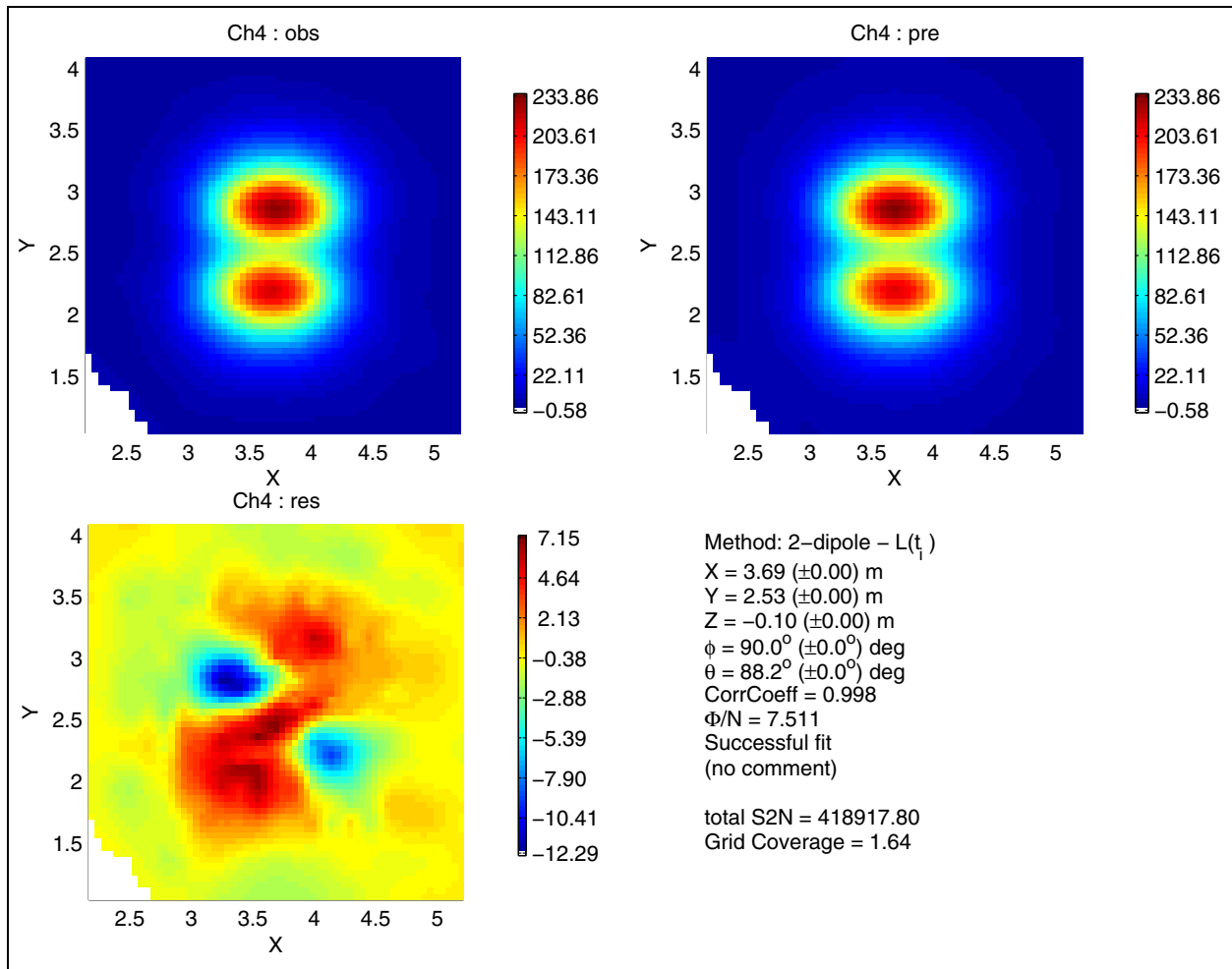
Figure 26. Two-dipole fit at time channel 4 to a horizontal 60-mm mortar 60 cm below the EM-61.

The time channels for the EM-61 are centered at 0.216, 0.366, 0.666, and 1.266 ms after pulse turn-off for channels 1 to 4, respectively. Even the relative amplitudes of the second time channel to the first time channel can be used to distinguish 50-caliber bullets from the other projectiles (Figure 27b). In contrast, the faster decay of the 20-mm projectiles compared to the 37-mm projectiles only becomes apparent at the fourth time channel (1.266 ms after pulse turn-off; Figure 27d). Even at that late time the difference between the decay rates of the two projectiles is quite small, indicating that it will not provide useful discriminatory information.
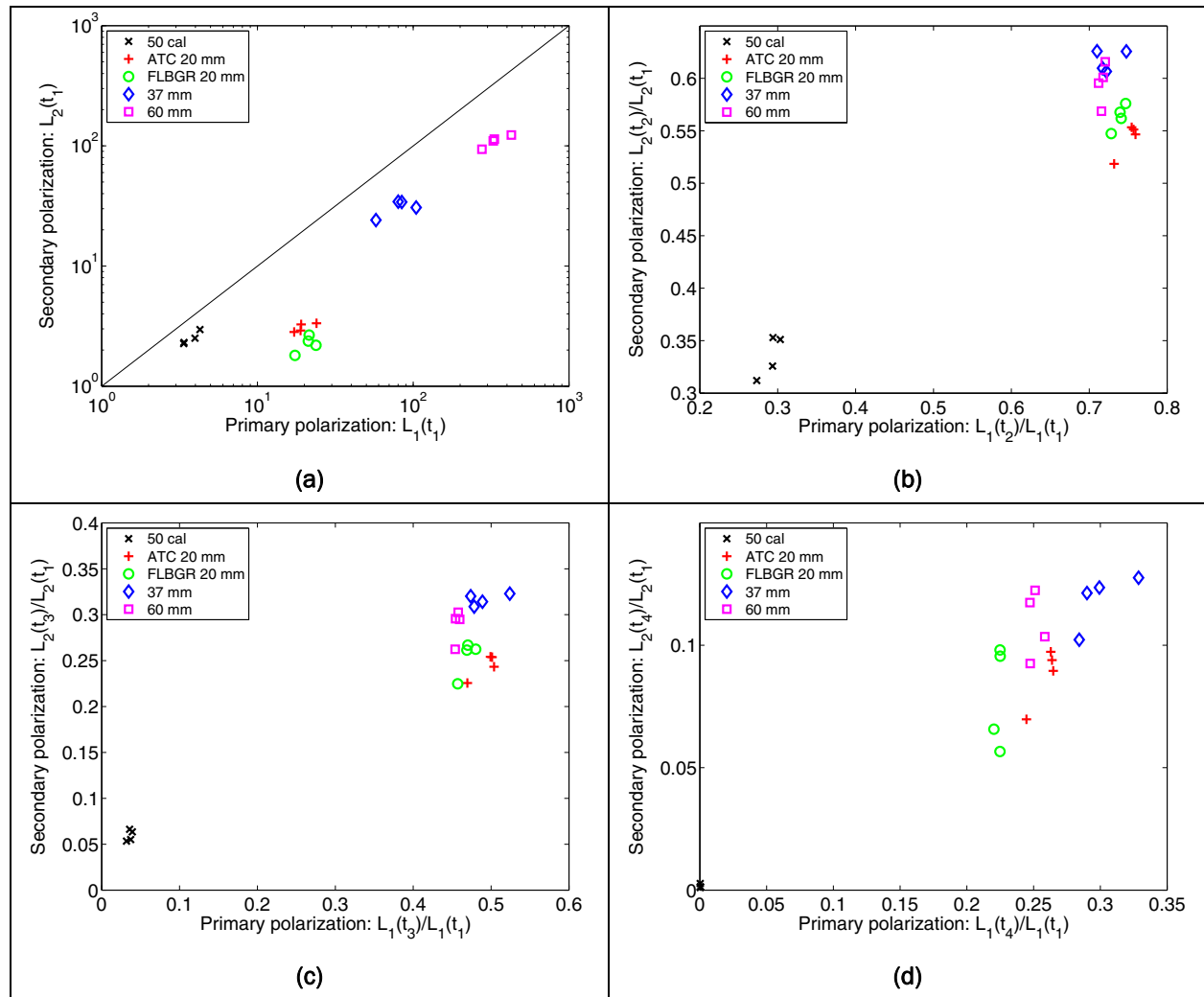
Figure 27. Parameters extracted from EM-61 test stand data. In each plot the parameter is plotted for both the primary and secondary polarizations: (a) Amplitude of the polarization at the first time channel (0.266 ms); (b) Ratio of polarizations at time channels 2 (0.366 ms) and 1; (c) Ratio of polarizations at time channels 3 (0.66 ms) and 1; and (c) Ratio of polarizations at time channels 4 (1.266 ms) and 1.

5.3. Inversion of GEM-3 data

To determine which features might be diagnostic between the different items, two-dipole instantaneous amplitude models were recovered (see Report 6) for each of the four sets of measurements made on each item with the GEM-3 during the 2006 data collection campaign (see Table 7). Figure 28 provides an example of the recovered dipole fit for the absolute value of the 90-Hz in-phase and quadrature response for an ATC BLU-26 oriented at a 45-degree dip, 30 cm below the GEM-3. There is very close agreement between the measured data and the dipole model, with the residuals typically less than 5 percent of the data values. Fits to the other GEM-3 test stand data are of comparable quality.
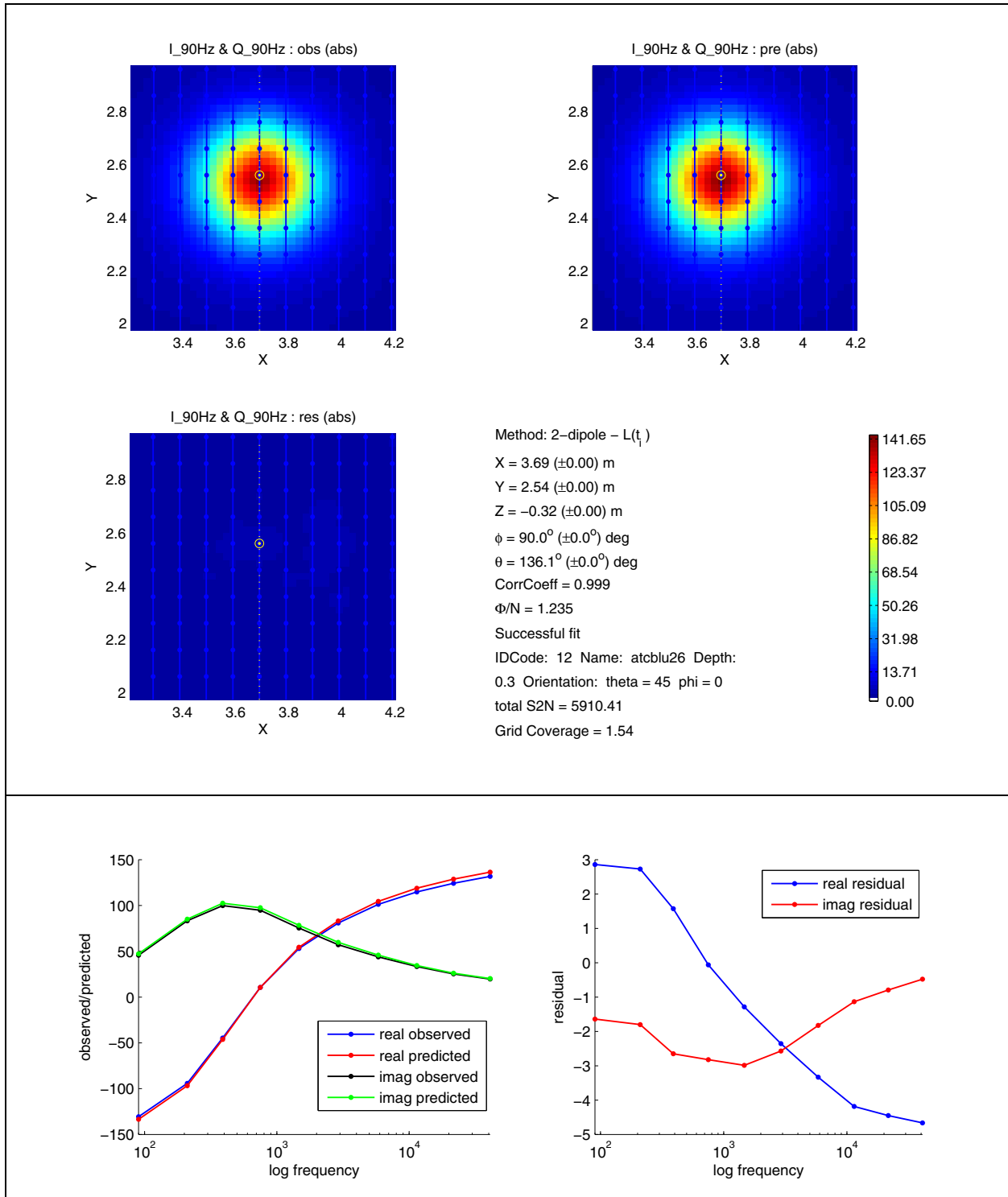
Figure 28. Two-dipole fit (absolute value of in-phase and quadrature) at 90-Hz frequency for an ATC BLU-26 ordnance 30 cm below the GEM-3. Top panel illustrates the measured and predicted data and the residual. The bottom panel illustrates the observed and predicted GEM-3 frequency spectra directly over the target and the residuals of the real and imaginary components. All GEM-3 units are in parts per million.

The axial and transverse instantaneous amplitudes L(U), of the two dipole inversions were subsequently fit to the following four-parameter model of Miller et al. (2001)

$$L(\omega) = k\left(s + \frac{(i\omega\tau)^c - 2}{(i\omega\tau)^c + 1}\right)$$

(2)

where:

ω = angular frequency
k = object amplitude
s = factor that controls the magnitude of asymptotes at high and low frequency
τ = response time-constant
c = parameter that controls the width of the in-phase peak response.

Figure 29 plots the transverse and axial values of k, τ, and s. There is good separation between most of the ordnance types in one or more of these parameter space plots. A plot of the axial-to-transverse amplitude ratio and against the crossover frequency[1] (Figure 29d) also reveals good separation between most of the various ordnance types.

The small-object discrimination scenario at the FLBGR (Report 9) provides a good example of how the dipole parameters might be used for discrimination. At the 20-mm Range Fan at FLBGR, the discrimination challenge is to distinguish between hazardous 37-mm projectiles and less hazardous 20-mm projectiles and 50-caliber bullets. There is a clear separation between all three items in the amplitude and time-constant plots (Figures 29a and 29b) and between the projectiles and the small arms in the s-parameter plot (Figure 29c). The s-parameter plot does not provide very good separation between the 20- and 37-mm projectiles. However, the good separation between the items in the amplitude and time-constant plots indicates that discrimination between all three items should be feasible with the GEM-3 (at least with accurately positioned data with a high signal-to-noise ratio (SNR)).

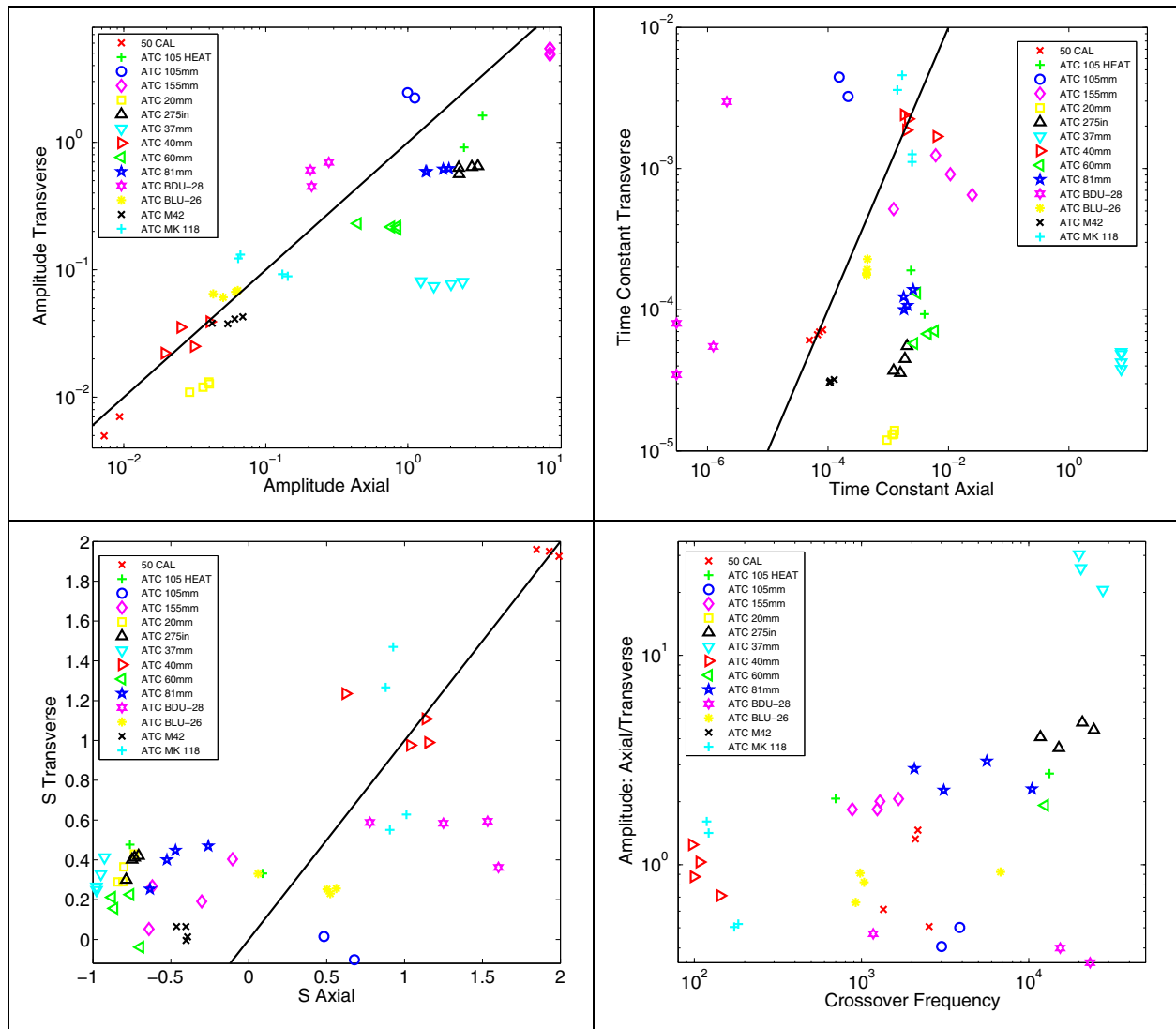[1] Where the amplitudes of the in-phase and quadrature components are equal.

Figure 29. Dipole parameters recovered from GEM-3 data collected over a number of different ordnance items. The solid line has equal transverse and axial parameter values.

6   Example Uses of the Test Stand Data

This chapter lists a number of applications where the test stand data have proven useful. These include

- The discrimination of 37-mm projectiles from 20-mm projectiles and 50-caliber bullets at the 20-mm Range Fan using the EM-63 and the GEM-3 (see text below and Report 9);
- Testing the improvement in discrimination performance between the cued and discrimination mode deployments of the EM-63 (see Report 5 in this series).
- The development of the Standardized Excitation Approach (see Report 6 in this series);
- The development of the Surface Magnetic Charge method (see Report 6 in this series);

EM-63 discrimination mode data were collected at the 20-mm Range Fan at FLBGR. The challenge at that site was to distinguish hazardous 37-mm projectiles from less dangerous 20-mm projectiles and 50-caliber bullets. Inversion of the data over each anomaly demonstrated that the amplitude of the polarization tensor was poorly constrained due to low SNR and insufficient position/orientation accuracy (Figure 30). However, the decay of the dominant polarization of the 37-mm projectiles was well con-strained and agreed closely with the response recovered from the test stand data (Figure 31). The relative decay of the 20-mm projectile was not as well constrained, but the recovered inversions tended to cluster around the curve obtained on the test stand. More details on this example can be found in Billings et al. (2007).

Figure 30. Polarization tensors recovered by inversion for all anomalies on the 20-mm Range Fan. Top left panel: Axial and transverse polarization tensors fit to test stand data over 20- and 37-mm projectiles. Top right panel: Dominant polarizations for 37-mm projectiles. Bottom left panel: Dominant polarization for 20-mm projectiles; Bottom right panel: Dominant polarizations for 50-caliber projectiles.

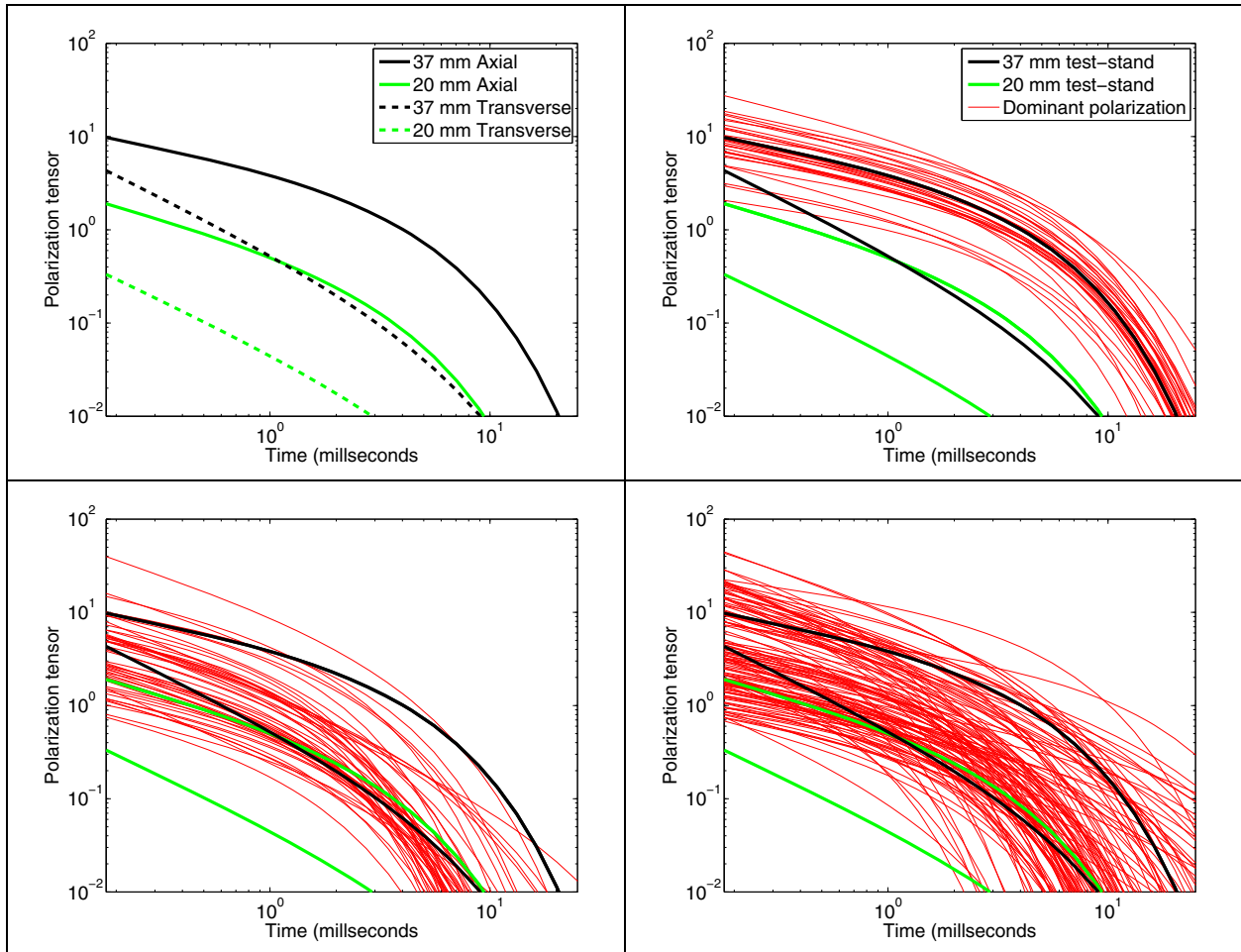Figure 31. Normalized polarization tensors recovered by inversion for all anomalies on the 20-mm Range Fan. Top left panel: Axial and transverse polarization tensors fit to test stand data over 20- and 37-mm projectiles. Top right panel: Dominant polarizations for 37-mm projectiles. Bottom left panel: Dominant polarization for 20-mm projectiles; Bottom right panel: Dominant polarizations for 50-caliber projectiles.
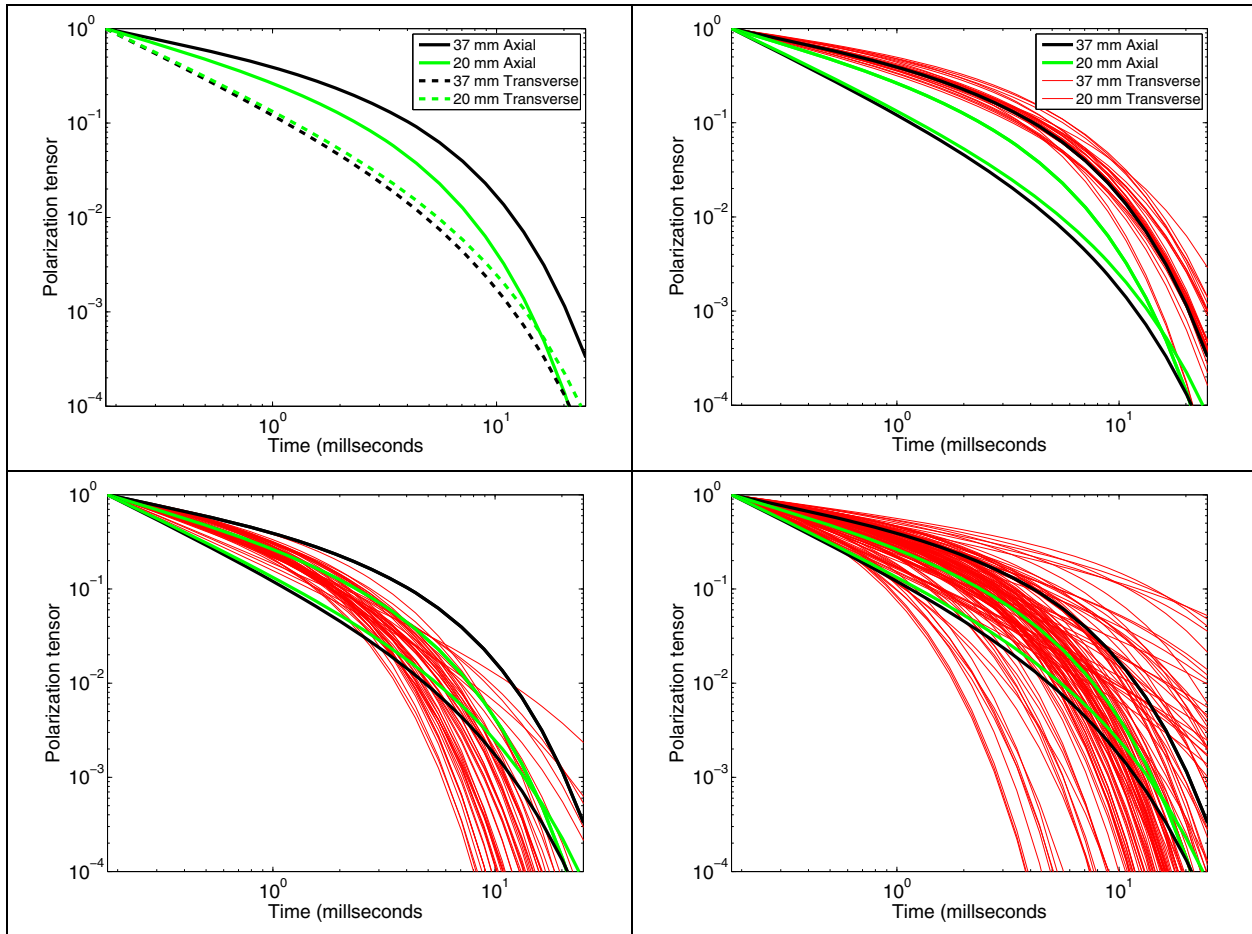
References

Bell, T. H., B. J. Barrow, and J. T. Miller. 2001. Subsurface discrimination using electromagnetic induction sensors. *IEEE Transactions on Geoscience and Remote Sensing* 39:1286-1293.

Billings, S. D., L. R. Pasion, L. Beran, D. W. Oldenburg, D. Sinex, and L. Song. 2007. Demonstration Report for the Former Lowry Bombing and Gunnery Range. Project 200504: Practical Discrimination Strategies for Application to Live Sites: Environmental Security Technology Certification Program.

Billings, S. D., C. Pasion, S. Walker, and L. Beran. 2006. Magnetic models of unexploded ordnance. IEEE Transactions of Geoscience and Remote Sensing 44:2115-2124.

Miller, J. T., T. H. Bell, J. Soukup, and D. Keiswetter. 2001. Simple phenomenological models for wide-band frequency domain electromagnetic induction. In *IEEE Transactions on Geoscience and Remote Sensing* 39:1294–1298.

Pasion, L. P., S. D. Billings, D. W. Oldenburg, and S. E. Walker. 2007. Application of a library based method to time domain electromagnetic data for the identification of unexploded ordnance. *Journal of Applied Geophysics* (in press).

Pasion, L. P., and D. W. Oldenburg. 2001. A discrimination algorithm for UXO using time domain electromagnetics. *Journal of Engineering and Environmental Geophysics* 28:91-102.

Appendix A: Investigation of Other Drift Removal Schemes

A.1. Current-based drift correction

The drift removal scheme employed thus far has been based on the drift of the response of the EM-63 with time. This seems reasonable since it can be seen from the top panel of Figure 7 that the static response (at the beginning and end of the survey) decreases by almost 7 mV. However, by examining the transmitter current values as a function of time (panel (b) in Figure A1), a rapid decrease in current occurred during the first 5 minutes of data collection. From the field notes recorded during data collection, the battery was being recharged immediately before the survey. This rapid decrease may be due to the battery returning to a steady state after charging. The first background measurement took place at the end of this decrease and as such the response may have been artificially high. Both plots in Figure Al show the extent of the survey measurements with a green square.

The transmitter current versus time plot in panel (b) in Figure A1 also shows a trend similar to the one observed in the time channel 1 response versus time. These observations suggest that a current-based drift correction may be more appropriate than a time-based correction. It is clear theoretically that the response and the transmitter current are related; however, upon export from the instrument, the data were normalized to a constant current of 15 amperes (A). Therefore, any further relationship between the transmitter current and the response is likely hardware related. While the exact cause of such a relationship is not known, it is likely related to the fact that the EM-63 transmitter and receiver electronics are powered by the same battery. Hence, as the survey proceeds, the voltage in the battery decreases. This will cause a decrease in the transmitter current, but it will also affect the behavior of the electronics associated with the receiver. As a first attempt at modeling and removing these effects, a linear drift model was adopted. The form of the drift assumed was defined as
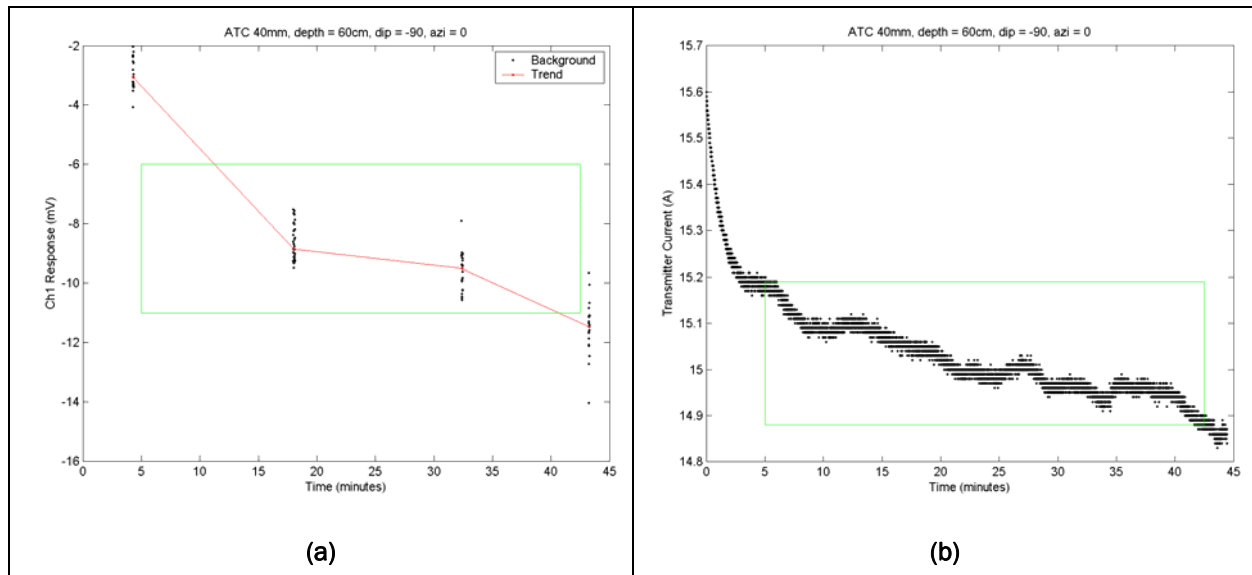
$$V = aI + b \qquad\qquad\qquad (A1)$$

Figure A1. Background channel 1 response and transmitter current as a function of time from the ATC 40 mm, depth = 60 cm, dip = -90°, and azimuth = 0° survey. In panel (a) the black dots indicate the data from the four static measurements and the red lines indicate the interpreted linear drift between the measurements. The green outline indicates the time of the survey. The channel 1 response is in millivolts, the transmitter current is in amperes, and the time is in minutes.

where V is the voltage, I is the transmitter current, and a and b are constants. The coefficients a and b were solved for each time channel using iteratively re-weighted least squares. The black dots and line in panel (a) of Figure A2 show the static measurement (1, 2) channel 1 data and the calculated best fitting drift model. The static measurements were used as a constant reference point; however, there are only four measurements throughout the entire survey. Assuming that the response at the edges of the test stand are zero, these data can be used to estimate the current drift. The red dots and line in panel (a) of Figure A2 show the edge of grid measurement data and the calculated best fitting drift model.

The best fit model from the static data has constants a = 25.43 and b = -390.29, whereas the edge data model has constants a = 19.42 and b = -305.34. It can be seen from panel (a) in Figure A2 that the larger value of the constant a from the static data is caused by the increased response at 15.2 A. These are the data from the first background measurement that took place just prior to surveying and may have been influenced by the recently charged battery. By including more data points, from within the survey, the results are less likely to be skewed by anomalous responses.
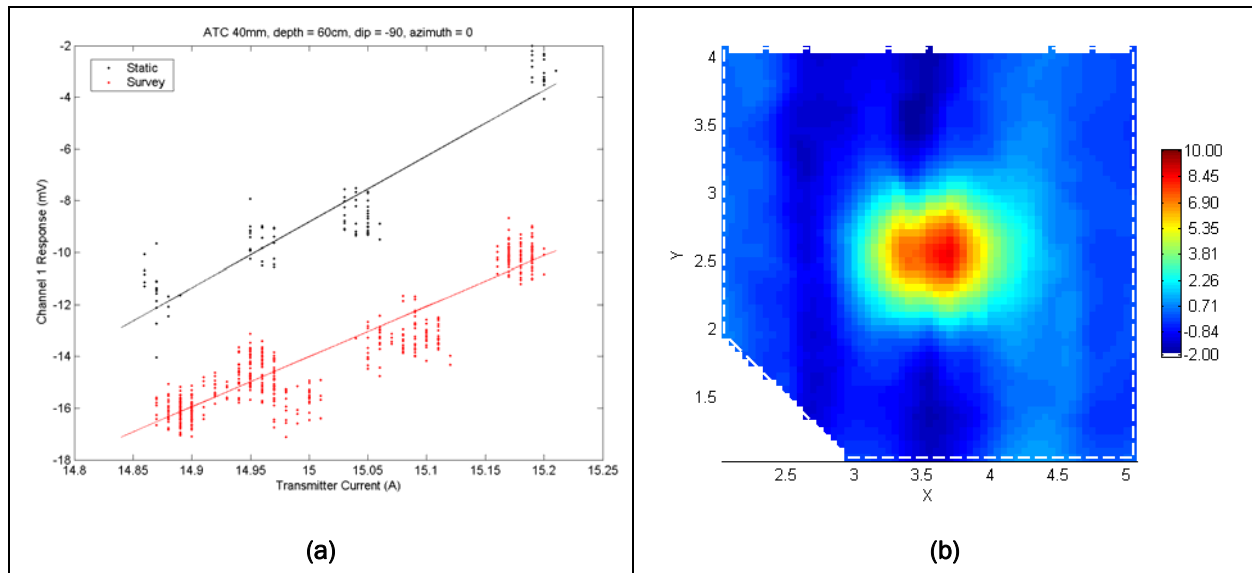
Figure A2. Panel (a): Background channel 1 response as a function of transmitter current. The black dots indicate the data from the four static measurements and the red dots indicate the data from the edges of the test stand. The black and red lines indicate the calculated drift models. The channel 1 response is in millivolts and the transmitter current is in amperes. Panel (b): Gridded image of transmitter current leveled channel 1 response data. All data from a survey over an ATC 40 mm, depth = 60 cm, dip = -90°, and azimuth = 0°.

The difference in the value of the constant *b* for the two models is due to the apparent dc shift between the two data sets. This is due to the fact that the static measurements were taken 1 m away from the #8 shot and its response is being detected by the instrument. Since the drift model predicted from the edge data appears to be less influenced by anomalous responses and provides a better estimate of a zero response it was selected to be used in the drift correction routine. Predicted current models and drift-corrected data for the ATC 20 mm at 40 cm and dip = 45; are shown in Figure A3.

While it appears that the current leveling scheme is adequately removing drift, there are still some features that are unaccounted for. In panel (a) of Figures A2 and A3, while the linear current drift model calculated from the edge data (red line) captures the general trend of the drift, the drift may in fact be measured by a higher order polynomial. Since the actual relationship between the transmitter current and the drift in response are not known, the time-based correction scheme appears to be a more viable option.
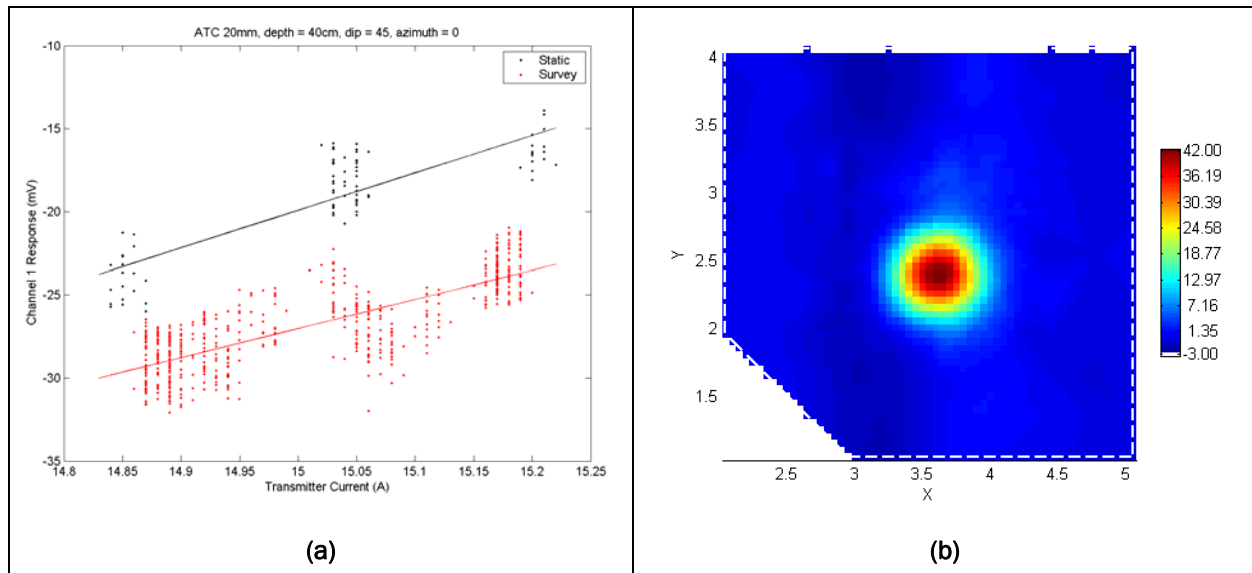
Figure A3. Panel (a): Background channel 1 response as a function of transmitter current. The black dots indicate the data from the four static measurements and the red dots indicate the data from the edges of the test stand. The black and red lines indicate the calculated drift models. The channel 1 response is in millivolts and the transmitter current is in amperes. Panel (b): Gridded image of transmitter current leveled channel 1 response data. All data from a survey over an ATC 20 mm, depth = 40 cm, dip = 45°, and azimuth = 0°.

A.2. Summary

It is possible to apply drift correction schemes that use either the change in response at each time channel as a function of time or as a function of transmitter current. Both methods have proven to be effective at removing the effects of drift from EM-63 data. However, since the relationship between the transmitter current and the drift in response is not known, the time-based drift correction routine was selected. By using the edge data, the time between interpolation points is reduced to less than 5 minutes in most cases and, therefore, the drift model is able to account for a greater amount of nonlinear drift than either the static time-based drift correction or the linearized current-based drift correction. Each EM-63 data set was drift-corrected using this technique. The EM-61 data were leveled using the same methodology.

Appendix B: Recovering GEM-3 Data Collected with an Incorrect Configuration File

When the GEM-3 was configured and running properly, the data collected by the GEM-3 were of a high quality. However, researchers encountered a recurring problem with configuration files. The Geophex manual clearly states a procedure to follow in order to ensure that the GEM-3 is operating properly. The first step is to collect a background measurement. While the sensor is away from any sources, the display is nulled. This should result in a reading with zero in-phase and quadrature at all frequencies. The next step is to place a ferrite rod near the sensor. The ferrite rod should produce a pure susceptibility response, which consists of zero quadrature and a constant negative in-phase at all frequencies. After performing these tests and observing the desired response, the GEM-3 is ready for surveying. Problems arise when the results of these measurements are not correct. The manual does not provide any trouble-shooting suggestions. The options left to the operator are to stop surveying or to carry on with measurements regardless. During test stand data acquisition, the problems were not noticed immediately and the result was that the GEM-3 was not configured correctly during the data acquisition process. After gaining more experience with the GEM-3, researchers discovered that these problems stem from using incorrect configuration files.

Each GEM-3 sensor has a particular configuration file associated with it. When the GEM-3 is operating with the proper configuration file, the measurements outlined in the manual provide the proper responses and surveying is successful. Besides setting the transmitting and receiving frequencies, detailed information is stored in the configuration file (Figures B1 and B2).

SYSTEM

Gem Configuration
System settings - Hardware settings

Sampling rate	192000	Battery DC resistance [ohm]	0.00022
Tx bitstream frequency	2	Battery potential to H-Br. [V]	12
Tx-coil inductance [µH]	77	FET DC resistance [ohm]	0.022
Tx coil DC resistance	0.388	Geometry factor	3500
Current Limit [A]	10	PowerLine-gauss coef.	1.96e-009
		Transm. Error	1e+006

< Back | Next > | Cancel

Corrections

Gem Configuration
View Corrections

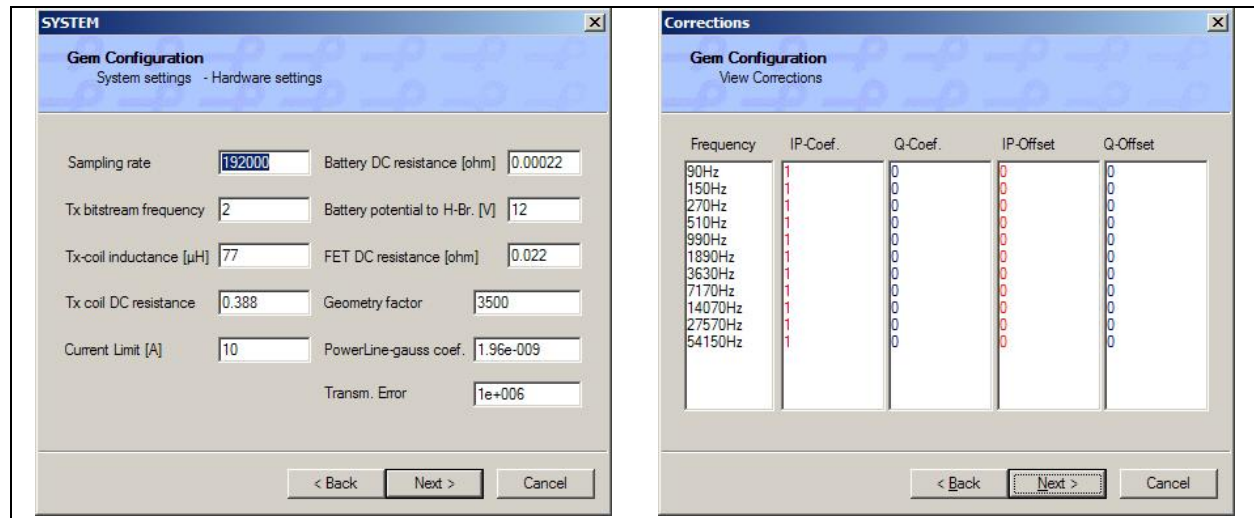| Frequency	IP-Coef.	Q-Coef.	IP-Offset	Q-Offset
90Hz	1	0	0	0
150Hz	1	0	0	0
270Hz	1	0	0	0
510Hz	1	0	0	0
990Hz	1	0	0	0
1890Hz	1	0	0	0
3630Hz	1	0	0	0
7170Hz	1	0	0	0
14070Hz	1	0	0	0
27570Hz	1	0	0	0
54150Hz	1	0		

< Back | Next > | Cancel

Figure B1. Details from the 40-cm GEM-3 configuration file used for data acquisition at the ERDC test stand. The left panel contains hardware settings and the right panel contains data corrections.

SYSTEM

Gem Configuration
System settings - Hardware settings

Sampling rate	96000	Battery DC resistance [ohm]	0.0022
Tx bitstream frequency	16	Battery potential to H-Br. [V]	12
Tx-coil inductance [µH]	170	FET DC resistance [ohm]	0.022
Tx coil DC resistance	0.56	Geometry factor	648.2
Current Limit [A]	12	PowerLine-gauss coef.	1.96e-009
		Transm. Error	1e+006

< Back | Next > | Cancel

Corrections

Gem Configuration
View Corrections

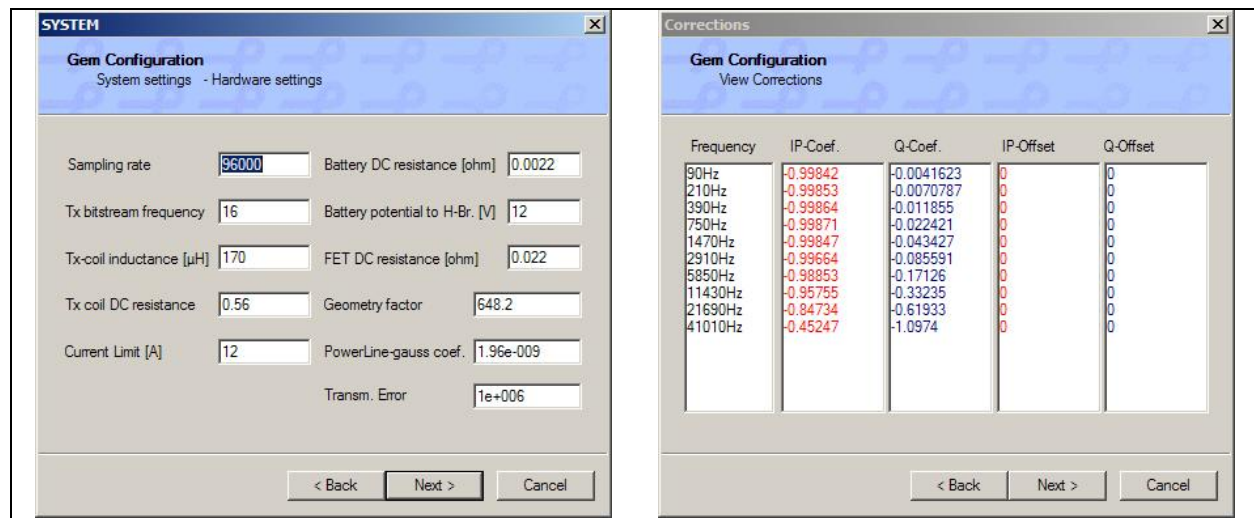| Frequency	IP-Coef.	Q-Coef.	IP-Offset	Q-Offset
90Hz	-0.99842	-0.0041623	0	0
210Hz	-0.99853	-0.0070787	0	0
390Hz	-0.99864	-0.011855	0	0
750Hz	-0.99871	-0.022421	0	0
1470Hz	-0.99847	-0.043427	0	0
2910Hz	-0.99664	-0.085591	0	0
5850Hz	-0.98853	-0.17126	0	0
11430Hz	-0.95755	-0.33235	0	0
21690Hz	-0.84734	-0.61933	0	0
41010Hz	-0.45247	-1.0974	0	0

< Back | Next > | Cancel

Figure B2. Details from a 40-cm GEM-3 configuration file used for data acquisition at the Ashland test plot. The left panel contains hardware settings and the right panel contains data corrections.

It is easy to see why problems arise when an incorrect configuration file is loaded into the GEM-3 console. The problem stems from the palmtop PC used for data logging. The WINGEMCE software on the palmtop over-writes the configuration file in the console depending upon the order in which the console and the palmtop are powered on. Without dwelling on why these problems occur, the result was that a large amount of data was collected with the incorrect configuration file. The more pressing issue is to determine if it is possible to transform any of the data into a useable form. For reference, Figure B3 contains a plot of the erroneous ferrite response from the test stand data and an estimate of the correct ferrite rod response.
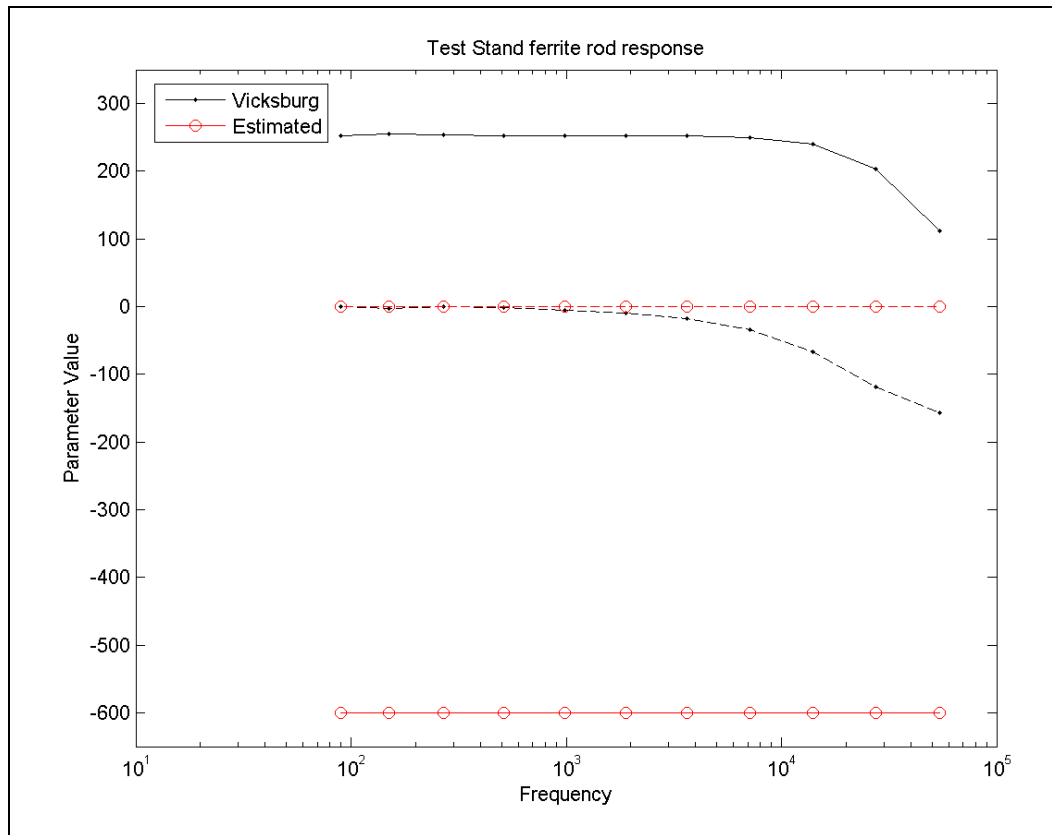
Figure B3. GEM-3 measurement over a ferrite rod from the test stand. Black lines indicate the data collected with an incorrect configuration file and the red lines indicate an estimate of the correct ferrite rod response. The solid lines are in-phase data and the dashed lines are quadrature.

It is clear that without a detailed knowledge of the design of the GEM-3 sensor, there is not much hope in using the hardware settings to correct the data in the GEM-3 configuration. However, the fact that the configuration file contains a set of coefficients and offsets that are applied to the in-phase and quadrature data at each frequency is more promising. A simple linear transformation was proposed to correct the data. The transformation is defined as

$$d_i^{corr} = a_i d_i^{err} + b_i \qquad\qquad (B1)$$

where d_i^{corr} and d_i^{err} are the ith corrected and erroneous measurements, a_i and b_i are i-th constants, and i has values from one to twice the number of frequencies. A transform with no b_i terms was also investigated. The transforms will be referred to as the single-parameter and two-parameter models.

Solving for the a_i and b_i values can be posed as a least-squares problem; however, at least two sets of correct and erroneous measurements over the same items are needed. In-air GEM-3 measurements were taken approximately 40 cm above a 12-in. solid steel cylinder oriented horizontally and vertically at the Ashland test plot. Test stand GEM-3 data were collected 50 cm above a similar cylinder oriented both horizontally and vertically. While the depth is not exactly the same, the character of the anomalies should be similar. Since an important feature of the data is the flat ferrite rod response, the measured ferrite rod response and the estimated values can be used as an extra data set. Two single-parameter models and two 2-parameter models were generated by solving the problem using the horizontal and vertical cylinder data alone and by using the cylinder and ferrite rod data. The results of applying the four transforms to the errone-ous data are shown in Figures B4, B5, and B6. The a_i and b_i values of the four transforms are plotted in Figures B7 and B8.

The best ferrite rod data fit comes from the two-parameter model recov-ered using all of the data (bottom right panel in Figure B6); however, the best vertical and horizontal cylinder data fits come from the two-parameter model recovered using just the cylinder data (bottom right panel in Figures B7 and B8). Closer inspection of the cylinder data plots shows that each of the recovered models is able to fit both the in-phase and quadrature data for the first six or seven frequencies. Even the models recovered using only the cylinder data predict the ferrite rod response at low frequency. The results of applying the one- and two-parameter models recovered from the cylinder-only data to an entire grid of test stand data are shown in Figures B9 and B10.

Aside from the presence of a response from the test stand itself, the data corrected using the two-parameter model in Figure B9 seem acceptable. At all frequencies the response away from the ordnance is close to zero. This is not the case in the data corrected with the two-parameter model. In Figure B10, the data in each panel have a different background value. After a closer look at the expression for the two-parameter model, this should not come as a surprise. The b parameter was calculated to fit the response directly over a target for a specific set (or sets) of data. However, when the correction is applied to a near zero background measurement, the back-ground will become equal to b. Close inspection shows that the back-ground values in the four panels of Figure B10 are equal to the corre-sponding b values in the lower left panel of Figure B7. These observations
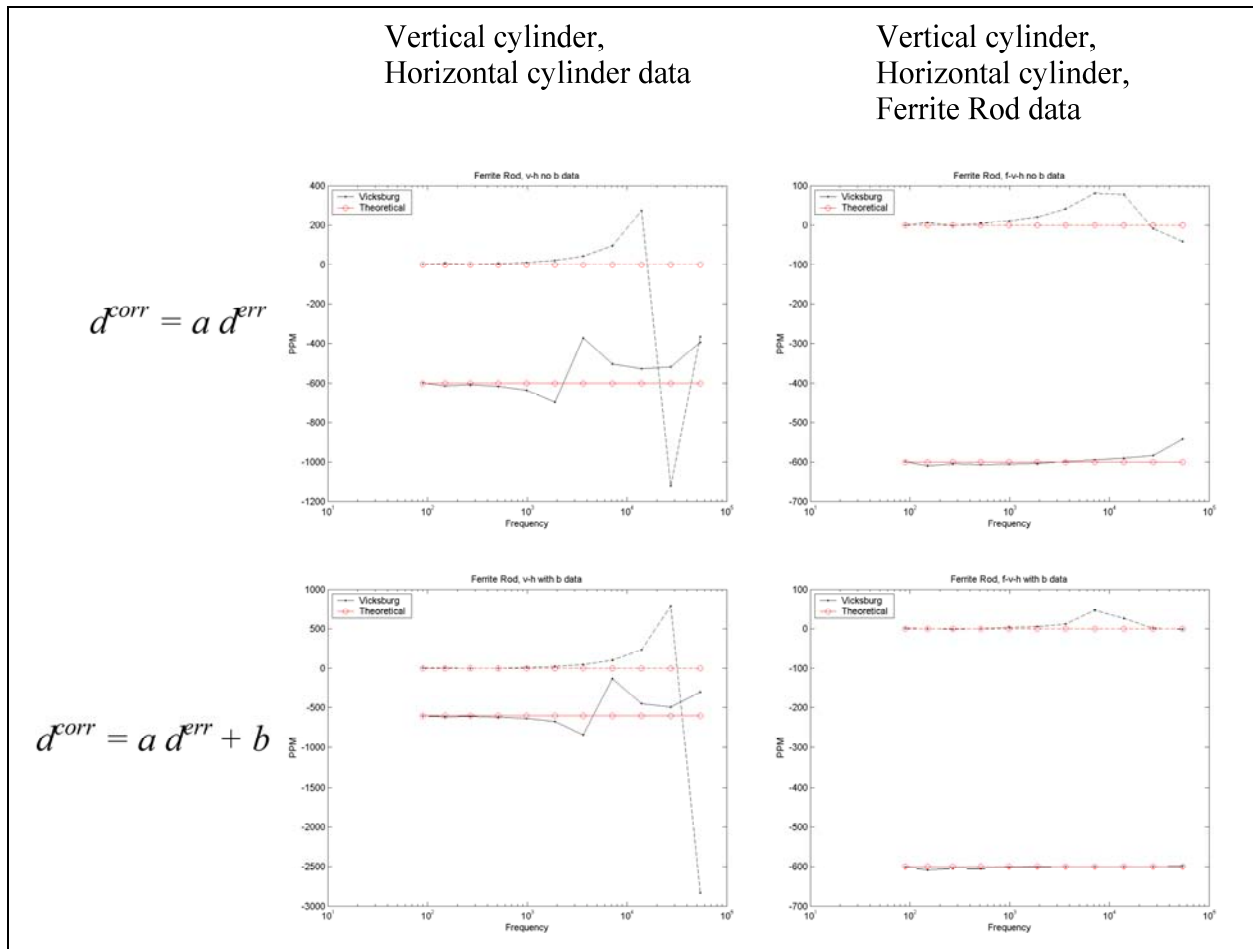
Figure B4. Comparison of corrected test stand data and theoretical data for the ferrite rod. The top row contains results from the single-parameter fitting, and the bottom row contains results from the two-parameter fitting. The left column contains data from fitting a model to the vertical and horizontal cylinder data, and the right column contains data from fitting a model to the vertical cylinder, horizontal cylinder, and ferrite rod data.

indicate that the two-parameter model should be used for the data transform. The data plots in Figures B7 and B8 show that the model recovered using the cylinder-only data fits the cylinder data better than the cylinder and ferrite rod data. Since this reasoning appears slightly circular, the researchers tested both transforms on a separate data set. The left panel of Figure B11 shows GEM-3 test stand data over a vertical 37-mm projectile that has been corrected using the transforms from the cylinder-only and cylinder and ferrite rod data. The right panel of Figure B11 shows an in-air measurement of a 37-mm projectile taken at the Ashland test plot.
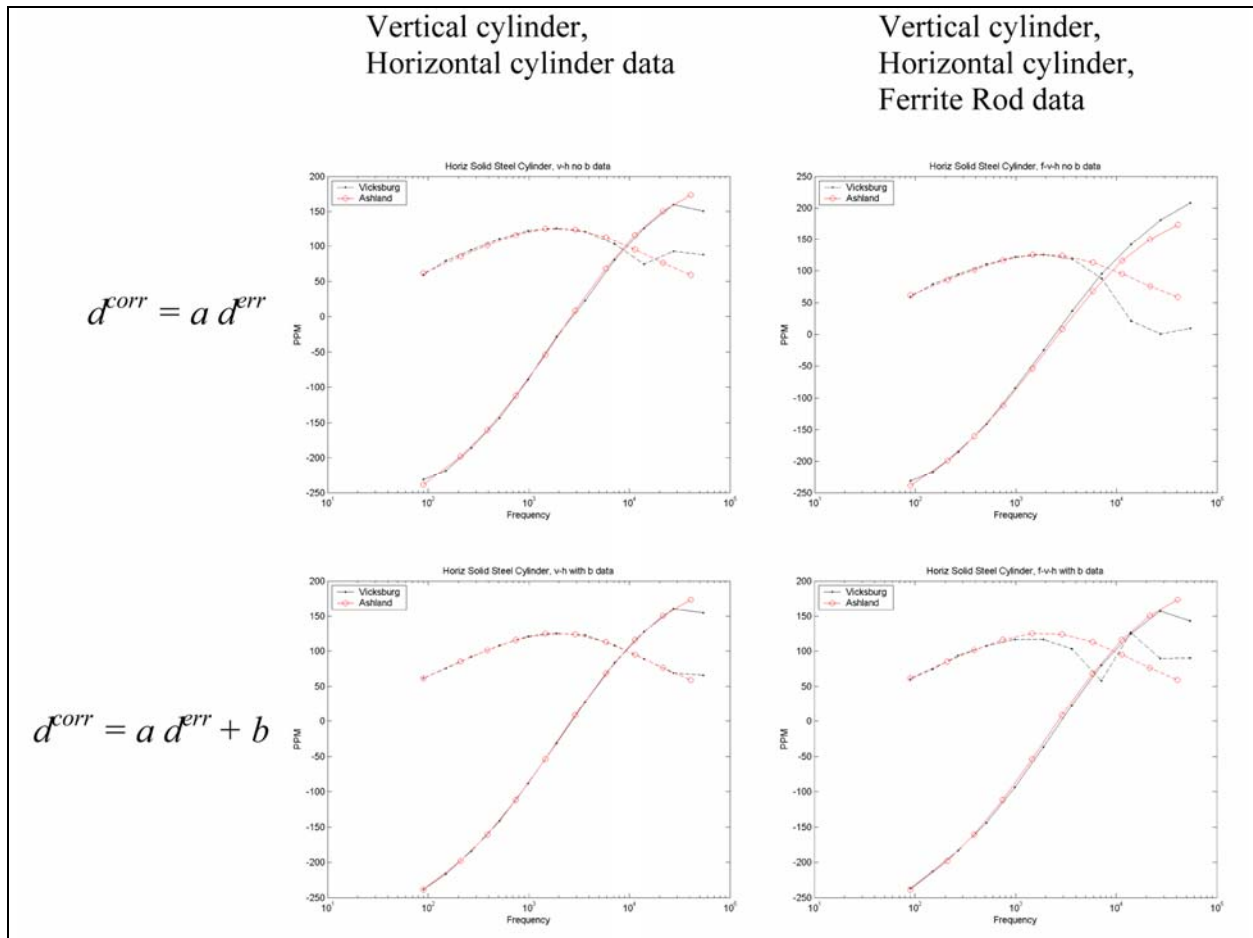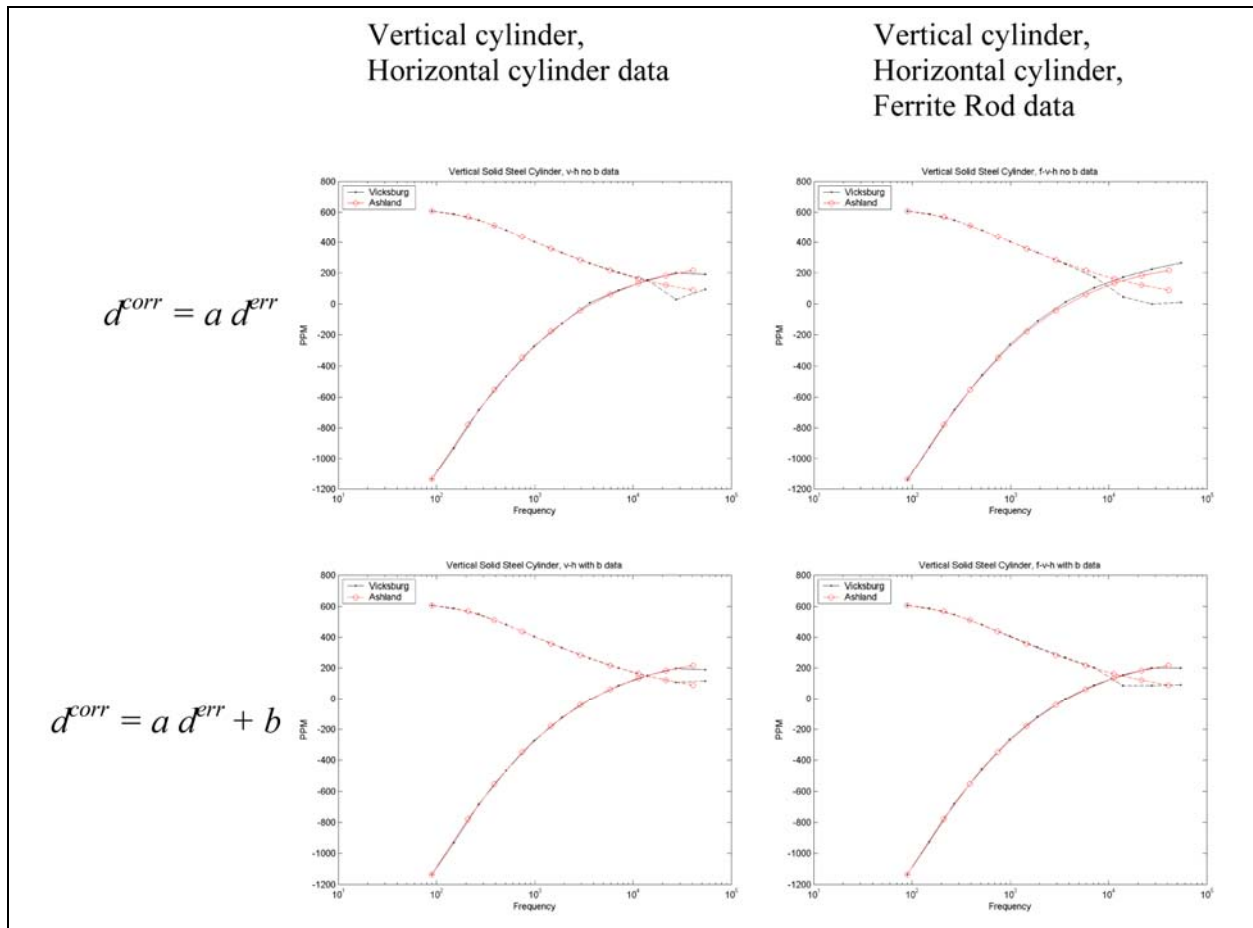
Figure B5. Comparison of corrected test stand data and Ashland data for horizontal solid steel cylinder. The top row contains results from the single-parameter fitting, and the bottom row contains results from the two-parameter fitting. The left column contains data from fitting a model to the vertical and horizontal cylinder data, and the right column contains data from fitting a model to the vertical cylinder, horizontal cylinder, and ferrite rod data.

The curves are plotted on different axes because the distance from the ordnance to the sensor for each data set is different (30 cm for test stand data and 10 cm for Ashland data) and, therefore, the amplitudes are quite different. However, the shapes of the curves should be (and are) similar. In panel (a) of Figure B11, the two corrected data sets match quite well up to approximately 10 kilohertz (kHz). Above this frequency the quadrature data diverge significantly. Overall, the data from the cylinder-only transform is smoother, and aside from a slight distortion above 10 kHz in the quadrature data the curves look similar to the curves in panel (b) of Figure B11. Aside from the amplitude, the major difference between the test stand and in-air data is the location of the in-phase-quadrature crossover point. In the test stand data the crossover is located near 10 kHz and in the Ashland data the crossover is at 41 kHz.

Figure B6. Comparison of corrected test stand data and Ashland data for vertical solid steel cylinder. The top row contains results from the single-parameter fitting, and the bottom row contains results from the two-parameter fitting. The left column contains data from fitting a model to the vertical and horizontal cylinder data, and the right column contains data from fitting a model to the vertical cylinder, horizontal cylinder, and ferrite rod data.

The single-parameter model recovered from the cylinder-only data was selected as the best transform. While all of the transforms appeared to break down at high frequency, this model provided the best overall data fit. It has yet to be determined if the corrected test plot data will be reliable enough to be used for testing modeling or inversion methodologies; however, it appears that the data will be good enough to provide a good spatial representation of the frequency-domain response of the ordnance that was measured.
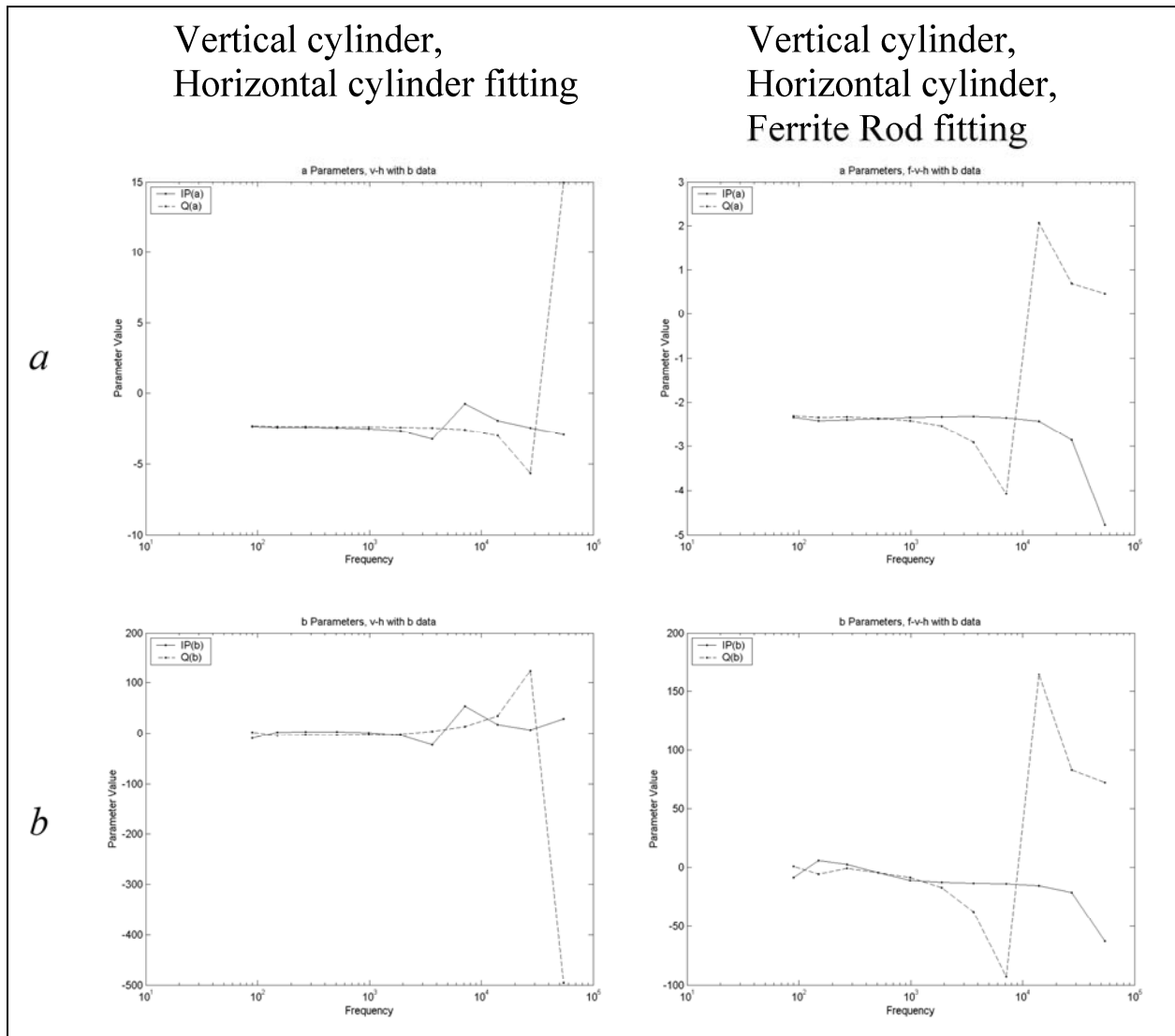
Figure B7. Plots of fit parameters a and b for the two-parameter models. The top row of plots contain the a parameter values, and the bottom row of plots contain the b parameter plots. The column on the left shows the models recovered from the cylinder-only data, and the column on the right shows the models recovered from the ferrite rod and cylinder data. The parameter values corresponding to the in-phase and quadrature data are plotted as solid lines, and dashed lines, respectively.
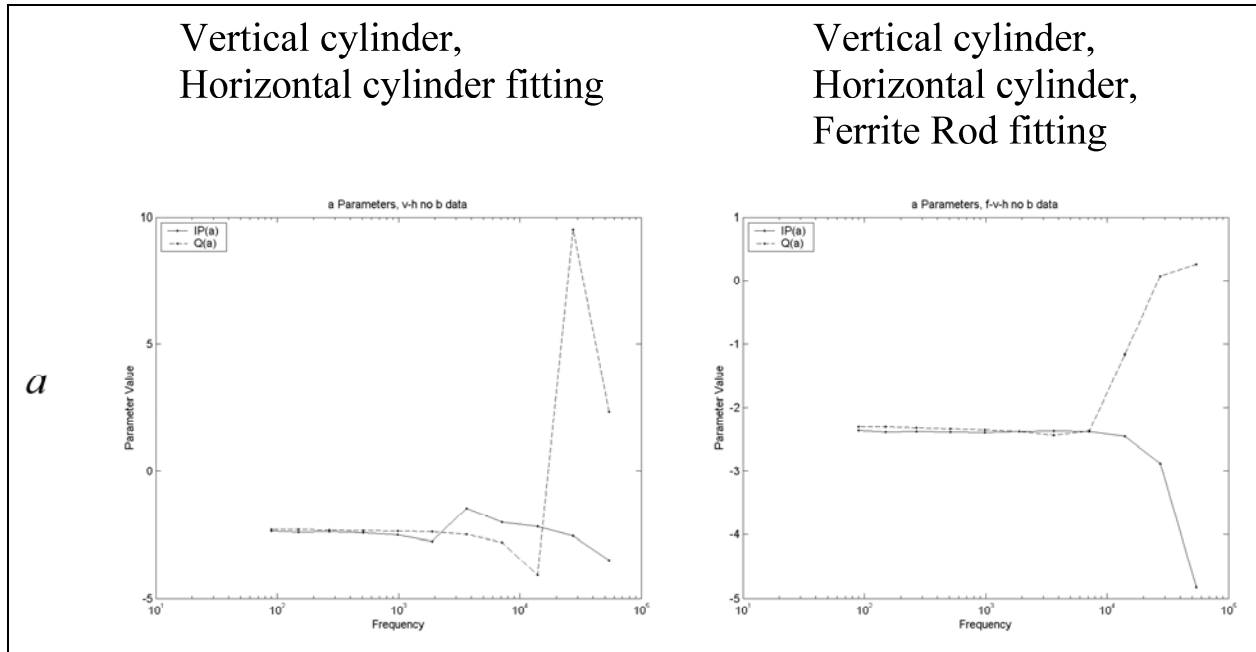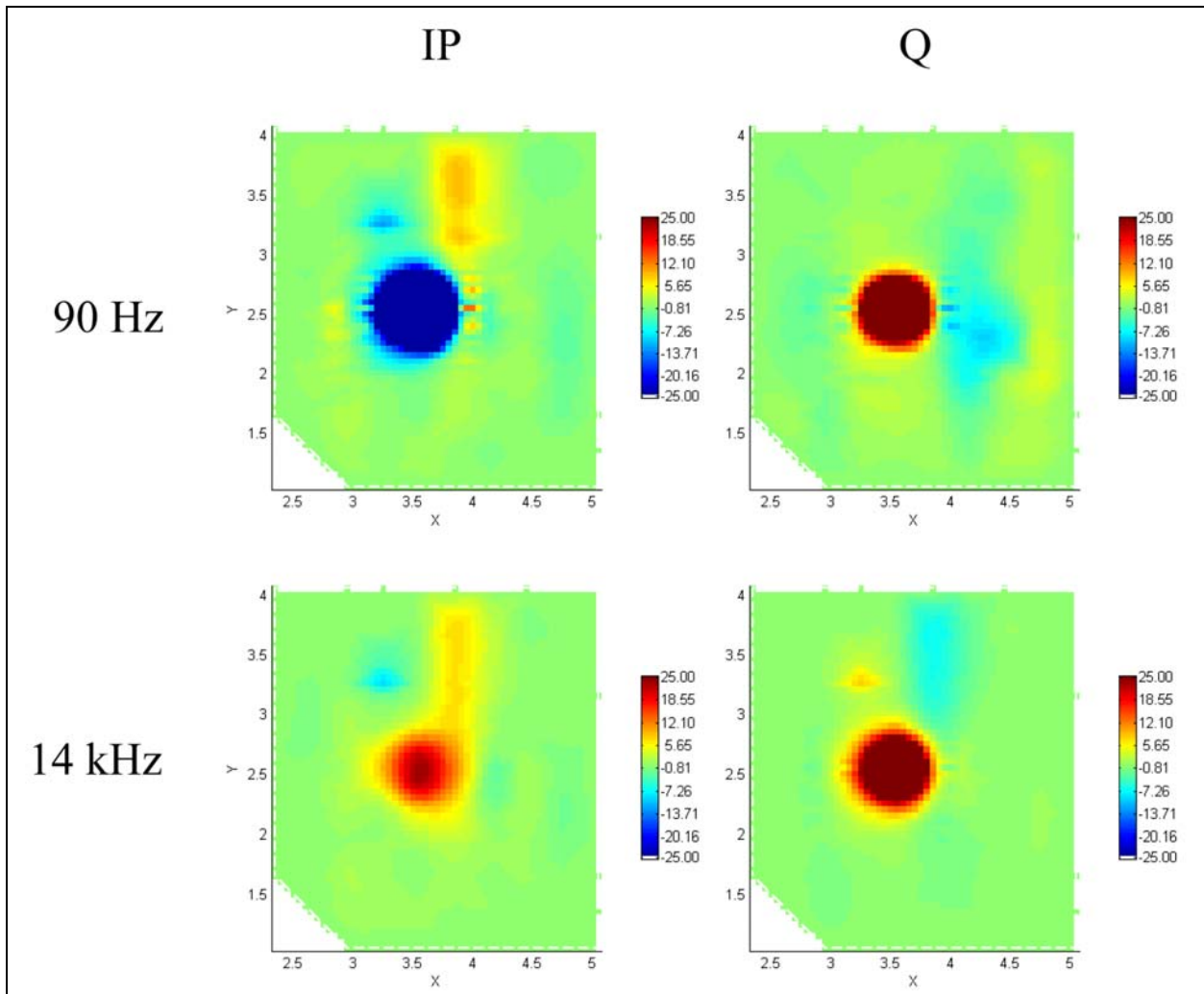
Figure B8. Plots of fit parameter a for the single-parameter models. The panel on the left shows the model recovered from the cylinder-only data, and the panel on the right shows the model recovered from the ferrite rod and cylinder data. The parameter values corresponding to the in-phase and quadrature data are plotted as solid lines and dashed lines, respectively.

Figure B9. Gridded data from test stand data corrected using the single-parameter model recovered from the cylinder data. Notice that the color scales on the plots are all the same to highlight the fact that the background value is zero for each measurement.
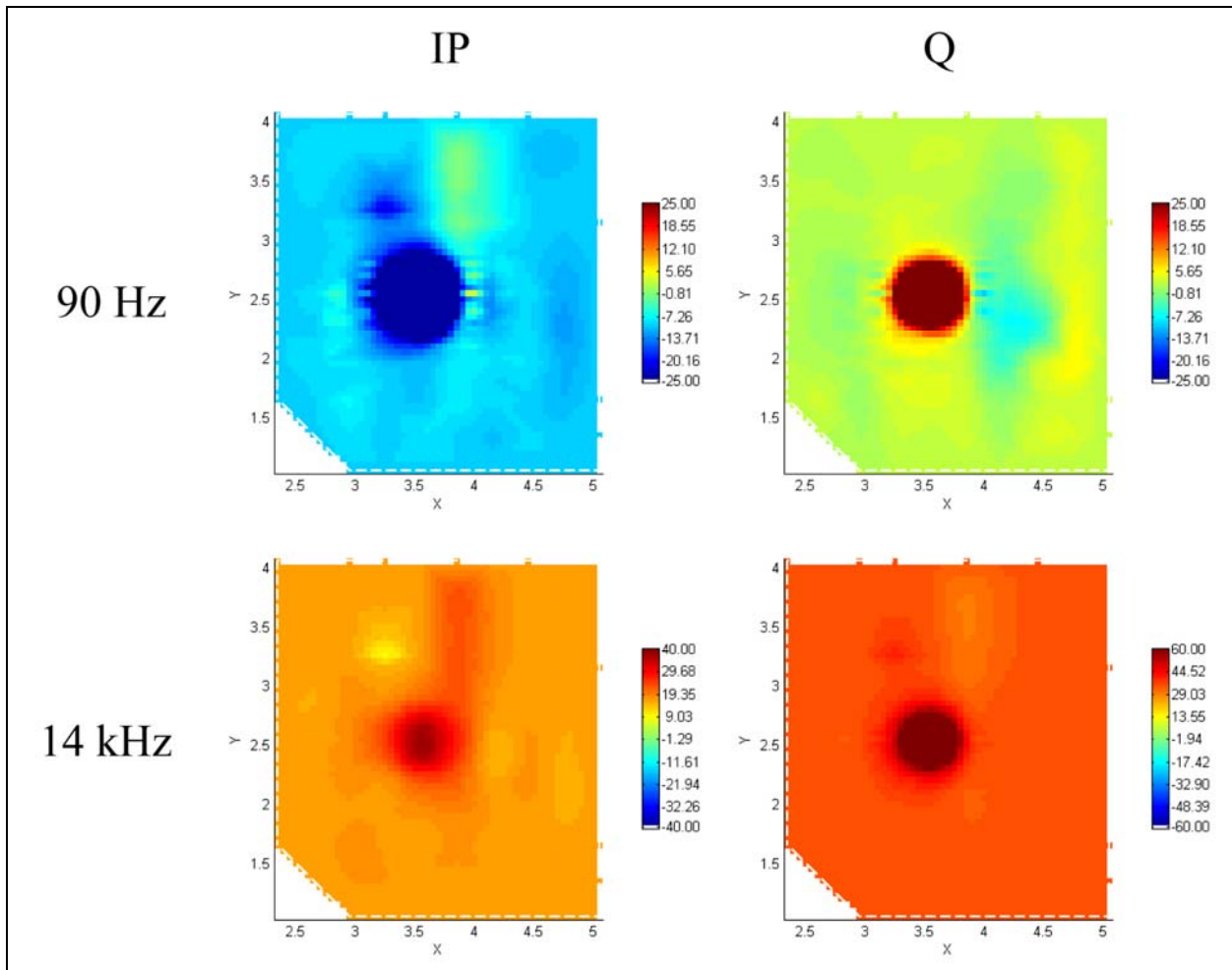
Figure B10. Gridded data from test stand data corrected using the two-parameter model recovered from the cylinder data. Notice that the color scales on the plots are different to highlight the fact that the background value is non-zero and varies with each measurement. The background value is approximately equal to the b value in the data fitting model.
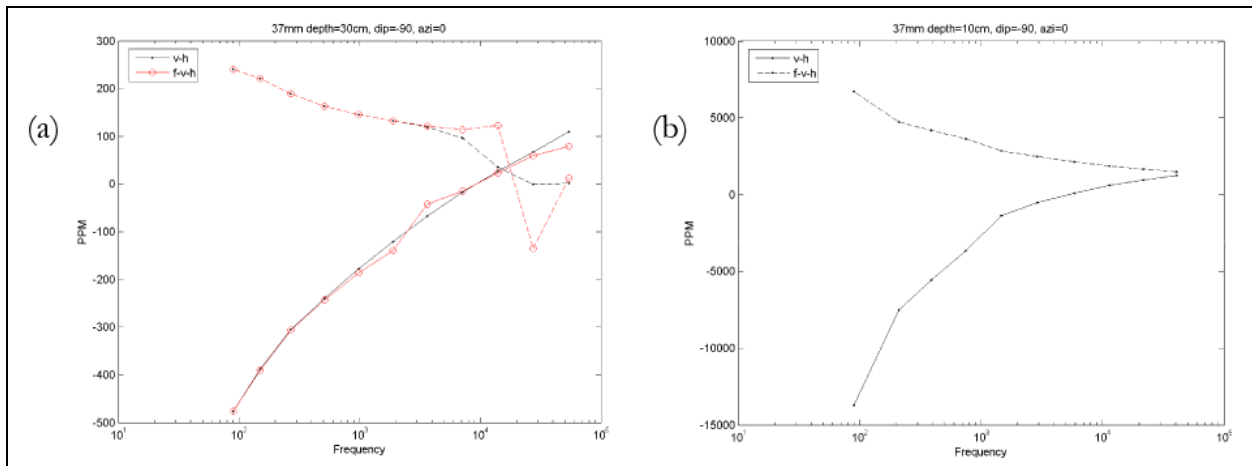
Figure B11. Comparison of corrected GEM-3 test stand 37-mm data and Ashland 37-mm data.

REPORT DOCUMENTATION PAGE

1. REPORT DATE *(DD-MM-YYYY)* September 2008	2. REPORT TYPE Report 3 of 9	3. DATES COVERED *(From - To)*

4. TITLE AND SUBTITLE UXO Characterization: Comparing Cued Surveying to Standard Detection and Discrimination Approaches: Report 3 of 9 – Test Stand Magnetic and Electromagnetic Measurements of Unexploded Ordnance	5a. CONTRACT NUMBER W912HZ-04-C-0039
	5b. GRANT NUMBER
	5c. PROGRAM ELEMENT NUMBER

6. AUTHOR(S) Stephen D. Billings, Leonard R. Pasion, Sean Walker, and Cathy Pasion	5d. PROJECT NUMBER
	5e. TASK NUMBER
	5f. WORK UNIT NUMBER

7. PERFORMING ORGANIZATION NAME(S) AND ADDRESS(ES) Sky Research, Inc. 445 Dead Indian Memorial Road Ashland, OR 97520	8. PERFORMING ORGANIZATION REPORT NUMBER ERDC/EL TR-08-34

9. SPONSORING / MONITORING AGENCY NAME(S) AND ADDRESS(ES) Headquarters, U.S. Army Corps of Engineers Washington, DC 20314-1000; U.S. Army Engineer Research and Development Center Environmental Laboratory 3909 Halls Ferry Road, Vicksburg, MS 39180-6199	10. SPONSOR/MONITOR'S ACRONYM(S)
	11. SPONSOR/MONITOR'S REPORT NUMBER(S)

12. DISTRIBUTION / AVAILABILITY STATEMENT

Approved for public release; distribution is unlimited.

13. SUPPLEMENTARY NOTES

14. ABSTRACT

This report describes a test stand data collection program that was designed to provide the highest possible quality magnetic and electromagnetic data over a suite of ordnance and calibration items. Each of the data points was precisely positioned and oriented, had low signal-to-noise ratio, and had minimal response from cultural or geologic sources. The test stand facility describes and an overview of the various geophysical instruments deployed, a description of the ordnance items measured, and a discussion of survey design and data collection are provided. Examples of how the data have been used in other parts of the overarching research project are also provided.

Test stand data were collected using a Geometries G822 cesium vapor magnetometer, Geonics EM-61 and EM-63 time-domain metal detectors and a Geophex GEM-3 frequency-domain detector. Measured items included 20-, 37-, 40-, 57-, 76-, 90- and 155-millimeter (mm) projectiles, a 2.75-in. rocket, 60- and 81-mm mortars, BLU-26, BLU28, MK118 Rockeye, and M42 submunitions, a 40-mm grenade, and a 105-mm HEAT round. A number of iron and aluminum cylinders, both hollow and solid, of different aspect ratio were also measured.

This is Report 3 in a series of nine reports prepared under project W912HZ-04-C-0039 "UXQ Characterization: Comparison of Cued-Surveying to Standard Detection and Standard Discrimination Approaches."

15. SUBJECT TERMS EMI sensors Frequency-domain electromagnetic induction(FEM)	Ground penetrating radar Time-domain electromagnetic induction (TEM) Total-field magnetics	Unexploded ordnance (UXO) UXO discrimination

16. SECURITY CLASSIFICATION OF:			17. LIMITATION OF ABSTRACT	18. NUMBER OF PAGES	19a. NAME OF RESPONSIBLE PERSON
a. REPORT UNCLASSIFIED	b. ABSTRACT UNCLASSIFIED	c. THIS PAGE UNCLASSIFIED		73	19b. TELEPHONE NUMBER *(include area code)*